

Numerical homogenization of second gradient, linear elastic constitutive models for cubic 3D beam-lattice metamaterials

Oliver Weeger^{a,*}

^a*Cyber Physical Simulation Group, Department of Mechanical Engineering, Technical University of Darmstadt, Dolivostrasse 15, 64293 Darmstadt, Germany*

Abstract

Generalized continuum mechanical theories such as second gradient elasticity can consider size and localization effects, which motivates their use for multiscale modeling of periodic lattice structures and metamaterials. For this purpose, a numerical homogenization method for computing the effective second gradient constitutive models of cubic lattice metamaterials in the infinitesimal deformation regime is introduced here. Based on the modeling of lattice unit cells as shear-deformable 3D beam structures, the relationship between effective macroscopic strain and stress measures and the microscopic boundary deformations and rotations is derived. From this Hill–Mandel condition, admissible kinematic boundary conditions for the homogenization are concluded. The method is numerically verified and applied to various lattice unit cell types, where the influence of cell type, cell size and aspect ratio on the effective constitutive parameters of the linear elastic second gradient model is investigated and discussed. To facilitate their use in multiscale simulations with second gradient linear elasticity, these effective constitutive coefficients are parameterized in terms of the aspect ratio of the lattices structures.

Keywords: Numerical homogenization, Generalized continuum mechanics, Second gradient linear elasticity, Lattice metamaterials, Multiscale simulation

1. Introduction

Additive manufacturing facilitates fabrication of heterogeneous structures with tailored complexity at topological, microstructural and material scales [1]. In particular, 3D printing of metamaterials such as cellular, foam- and lattice-type microstructures allows the variation and grading of their topology, density, or material constitution in order to locally adapt mechanical and functional properties [2, 3]. Thus, the fabrication of beam-type lattice structures and metamaterials with functionalized behavior has received increasing attention in recent years. For instance, approaches such as the customization of lightweight lattice structures in selective laser melting [4], grayscale printing of functionally graded lattice structures [5], design and manufacturing of soft lattices with tailored mechanical behavior [6, 7], magnetic field-responsive metamaterials [8], and multiscale metallic metamaterials with hierarchical lattice-substructures [9] have been presented.

For multiscale modeling of cellular materials, it is typically assumed that a representative volume element (RVE, for stochastic foams) or a periodically repeated unit cell (RUC, for lattices) exists, which can be used to characterize the effective behavior of a microstructure [10, 11]. Furthermore, it is assumed that the microstructure is several orders of magnitude smaller than the macroscopic domain, i.e., there is a *separation of scales* between macro- and microscales, such that asymptotic homogenization methods can be used to determine the effective material properties of the microstructure and model the macrostructure as a continuum [12, 13].

*Corresponding author

Email address: weeger@cps.tu-darmstadt.de (Oliver Weeger)

These multiscale modeling approaches have been widely applied to open-cell, beam lattice-type cellular solids. At the microscale, or one might rather consider it the mesoscale, lattice unit cells and struts are usually either modeled as trusses, beams, or solid continua and then either analytical or numerical methods are used to homogenize the linear elastic material properties of the unit cells and characterize their dependence on cell topology and its aspect ratio (strut diameter over unit cell size) or relative density [11, 14–19]. In the context of additive manufacturing, a number of recent works have also been considering effects of node geometries and manufacturing imperfections on the resulting effective properties [20–24]. For generative design of lattice structures, homogenization-based topological multiscale design optimization methods have also been developed [25–29]. Usually, infinitesimal strains and linear elastic (multiscale) modeling are considered sufficient, since lattice structures are particularly relevant for lightweight designs made from metals with small fracture strains. Recent works also address soft, deformable lattice structures made from polymers and elastomers, which can exhibit large deformations and buckling [?].

Practical applications and multiscale topology optimization often yield lattice designs with slender, beam-like macroscopic structures that consist of only few unit cells in at least one spatial direction. Thus, the micro and macro scales are not properly separated and small features and localized loading conditions can result in size, localization and boundary effects, which play a crucial role for multiscale modeling of lattice structures and mechanical metamaterials in general [30–32]. Generalized continuum mechanical theories, such as second gradient or strain gradient models, micropolar (Cosserat) or micromorphic continua, which introduce hyperstresses or couple stresses, can describe these size and localization effects that cannot be appropriately modeled by the classical Cauchy theory [33, 34]. Second or strain gradient theories have already been shown to capture size effects of small scale structures well [35], and have, for instance, also been used in fracture and plasticity [36, 37].

However, generalized continuum mechanical theories require additional constitutive tensors and parameters, which are typically non-intuitive and difficult to obtain experimentally. Thus, homogenization methods have been developed to compute the relevant parameters numerically for a given microstructure [38–44]. However, the application of high-order boundary conditions still remains a challenge [45? , 46]. Recently, due to the increasing interest in metamaterials, several works addressed homogenization for beam microstructures. A discrete homogenization method for periodic Euler–Bernoulli beam structures was introduced in [47, 48] and used to determine yield strength. Asymptotic homogenization of micropolar continuum models for beam lattices was presented in [49]. Size effects in 2D lattice structures were investigated using micropolar elasticity in [50], however, in this case, the multiscale simulations tended to under-predict the behavior of lattices with low scale-separation compared to full-scale simulations. Furthermore, homogenization and strain gradient models have been developed for pantographic lattice structures [51], as well as beam microstructures in the context of continuum and plate multiscale simulation methods [52, 53]. A micropolar continuum model for 2D truss microstructures undergoing finite deformations has been obtained in [54] and a micromorphic model for dynamics of metamaterials in [55]. For 2D and 3D auxetic structures, homogenization of a nonlinear micropolar continuum model was developed in [56]. To the best of the author’s knowledge, no prior works have so far addressed multiscale modeling of 3D beam-lattice structures and metamaterials using higher gradient continua and investigated the dependence of the homogenized constitutive models on the microstructural parameters.

Based on prior works on modeling of 2D microstructures as higher gradient continua, we here employ Mindlin’s second gradient linear elastic theory [57, 58] for the macroscopic continuum modeling. The linear elastic constitutive tensors for the stresses and hyperstresses are obtained via numerical homogenization of lattice unit cells, which are subjected to periodic boundary conditions and constitutive parameters are calculated from the Hill–Mandel equivalence of macro- and microscopic potential energies, see [42]. For this purpose, the unit cells are modeled mechanically as shear-deformable 3D beam structures and numerically discretized by an isogeometric collocation method [59] (though any other suitable method could be used).

This manuscript is organized as follows. After this introductory section, we discuss the macroscopic modeling using second gradient linear elasticity for infinitesimal deformations and strains in Section 2. Then, the microscale beam model of lattice unit cells and its discretization with isogeometric collocation are detailed in Section 3. The homogenization method that connects both, the macro and micro scales, by obtaining the effective constitutive coefficients is introduced in Section 4. In Section 5, this multiscale simulation

framework is then applied to numerically homogenize various types of beam-lattice microstructures. The properties of the constitutive tensors, in particular their dependence on the microstructural parameters and stretch- or bending-dominated deformation behavior, are investigated. Finally, a summary of the methods and results is presented in Section 6.

2. Macroscale modeling

In this section, the macroscopic modeling approach using linear second gradient elasticity in 3D is outlined. For a compact notation, most of the physical relations are given in symbolic tensor notation. For clarification of specific quantities, index notation is used, where indices take the values of 1,2,3, and Einstein's summation convention is applied.

In the framework of classical continuum mechanics, it is assumed that the potential energy $\Psi : \Omega \rightarrow \mathbb{R}$ stored in an elastic continuum given by the domain $\Omega \subset \mathbb{R}^3$, here the macroscopic continuum, depends (only) on the first gradient of the displacement field $\mathbf{u} : \Omega \rightarrow \mathbb{R}^3$:

$$\Psi = \Psi(\nabla \mathbf{u}). \quad (1)$$

In linear elasticity, the theory is restricted to infinitesimal displacements and the strain energy is formulated in terms of the infinitesimal strain tensor $\boldsymbol{\varepsilon} : \Omega \rightarrow \mathbb{R}^{3 \times 3}$, i.e., the symmetric part of the deformation gradient:

$$\boldsymbol{\varepsilon}(\mathbf{x}) = \frac{1}{2} (\nabla \mathbf{u}(\mathbf{x}) + \nabla \mathbf{u}(\mathbf{x})^\top), \quad \varepsilon_{ij} = \frac{1}{2} (u_{i,j} + u_{j,i}). \quad (2)$$

Linear second gradient elasticity requires also the second gradient of the displacement field $\boldsymbol{\kappa} : \Omega \rightarrow \mathbb{R}^{3 \times 3 \times 3}$, i.e., a third order tensor [57, 60, 61]:

$$\boldsymbol{\kappa}(\mathbf{x}) = \nabla^2 \mathbf{u}(\mathbf{x}), \quad \kappa_{ijk} = u_{i,jk}. \quad (3)$$

The strain energy functional of second gradient elasticity is then formulated in terms of both $\boldsymbol{\varepsilon}$ and $\boldsymbol{\kappa}$:

$$\begin{aligned} \Psi = \Psi(\boldsymbol{\varepsilon}, \boldsymbol{\kappa}) &= \frac{1}{2} \boldsymbol{\varepsilon} : \mathbb{C} : \boldsymbol{\varepsilon} + \frac{1}{2} \boldsymbol{\kappa} : \mathbb{D} : \boldsymbol{\kappa} + \boldsymbol{\varepsilon} : \mathbb{M} : \boldsymbol{\kappa} \\ &= \frac{1}{2} \varepsilon_{ij} C_{ijkl} \varepsilon_{kl} + \frac{1}{2} \kappa_{ijk} D_{ijklmn} \kappa_{lmn} + \varepsilon_{ij} M_{ijklmn} \kappa_{lmn}, \end{aligned} \quad (4)$$

where $\mathbb{C} \in \mathbb{R}^{3 \times 3 \times 3 \times 3}$ is the classical, fourth-order elastic constitutive tensor, $\mathbb{D} \in \mathbb{R}^{3 \times 3 \times 3 \times 3 \times 3 \times 3}$ the sixth-order second gradient constitutive tensor, and $\mathbb{M} \in \mathbb{R}^{3 \times 3 \times 3 \times 3 \times 3 \times 3}$ a fifth-order coupling tensor. Here, we focus on cubic lattice microstructures, which are centro-symmetric and thus the coupling tensor \mathbb{M} vanishes [41, 61].

The classical Cauchy stress tensor $\boldsymbol{\sigma} : \Omega \rightarrow \mathbb{R}^{3 \times 3}$ and the hyperstress or double stress tensor $\boldsymbol{\tau} : \Omega \rightarrow \mathbb{R}^{3 \times 3 \times 3}$ of the second gradient continuum are then obtained by differentiation of the strain energy density:

$$\begin{aligned} \boldsymbol{\sigma}(\mathbf{x}) &= \frac{d\Psi}{d\boldsymbol{\varepsilon}} = \mathbb{C} : \boldsymbol{\varepsilon}(\mathbf{x}), & \sigma_{ij} &= C_{ijkl} \varepsilon_{kl}, \\ \boldsymbol{\tau}(\mathbf{x}) &= \frac{d\Psi}{d\boldsymbol{\kappa}} = \mathbb{D} : \boldsymbol{\kappa}(\mathbf{x}), & \tau_{ijk} &= D_{ijklmn} \kappa_{lmn}. \end{aligned} \quad (5)$$

Besides the symmetry of the Cauchy stress tensor, $\sigma_{ij} = \sigma_{ji}$, the symmetry $\tau_{ijk} = \tau_{ikj}$ can be imposed on the hyperstress tensor [61], and with the symmetries of the strain and second gradient tensors, $\varepsilon_{ij} = \varepsilon_{ji}$, $\kappa_{ijk} = \kappa_{ikj}$, the following symmetries apply to the constitutive tensors:

$$C_{ijkl} = C_{jikl} = C_{klij}, \quad D_{ijklmn} = D_{ikjlmn} = D_{lmnijk}. \quad (6)$$

Thus, the number of independent coefficients of the constitutive tensors reduces from $3^4 = 81$ to 21 for \mathbb{C} and from $3^6 = 729$ to 171 for \mathbb{D} . Furthermore, we are here restricted to microstructures with cubic anisotropy, see Sect. 3.1 and Fig. 2, for which the symmetry group consists of rotations by 90° around their three

perpendicular axis and centro-symmetry. Altogether, this reduces the number of independent parameters of \mathbb{C} to 3 and of \mathbb{D} to 11 [61].

Exploiting all these symmetries, for implementation purposes, the well-known Voigt matrix-vector notation is used for the formulation of the “first-order” constitutive equation:

$$\boldsymbol{\sigma} = \mathbb{C} : \boldsymbol{\varepsilon} \quad \Leftrightarrow \quad \tilde{\boldsymbol{\sigma}} = \tilde{\mathbb{C}} \cdot \tilde{\boldsymbol{\varepsilon}}, \quad (7)$$

with

$$\begin{aligned} \tilde{\boldsymbol{\sigma}} &= (\sigma_{11} \quad \sigma_{22} \quad \sigma_{33} \quad \sigma_{23} \quad \sigma_{13} \quad \sigma_{12})^\top \in \mathbb{R}^6, \\ \tilde{\boldsymbol{\varepsilon}} &= (\varepsilon_{11} \quad \varepsilon_{22} \quad \varepsilon_{33} \quad 2\varepsilon_{23} \quad 2\varepsilon_{13} \quad 2\varepsilon_{12})^\top \in \mathbb{R}^6, \end{aligned} \quad (8)$$

and $\tilde{\mathbb{C}} \in \mathbb{R}^{6 \times 6}$. Likewise, for the “second-order” constitutive equation a Kelvin–Mandel-like notation is used:

$$\boldsymbol{\tau} = \mathbb{D} : \boldsymbol{\kappa} \quad \Leftrightarrow \quad \tilde{\boldsymbol{\tau}} = \tilde{\mathbb{D}} \cdot \tilde{\boldsymbol{\kappa}}, \quad (9)$$

with

$$\tilde{\boldsymbol{\tau}} = \begin{pmatrix} \tau_{111} \\ \sqrt{2}\tau_{212} \\ \sqrt{2}\tau_{313} \\ \tau_{122} \\ \tau_{133} \\ \tau_{222} \\ \sqrt{2}\tau_{121} \\ \sqrt{2}\tau_{323} \\ \tau_{211} \\ \tau_{233} \\ \tau_{333} \\ \sqrt{2}\tau_{131} \\ \sqrt{2}\tau_{232} \\ \tau_{311} \\ \tau_{322} \\ \sqrt{2}\tau_{123} \\ \sqrt{2}\tau_{231} \\ \sqrt{2}\tau_{312} \end{pmatrix} \in \mathbb{R}^{18}, \quad \tilde{\boldsymbol{\kappa}} = \begin{pmatrix} \kappa_{111} \\ \sqrt{2}\kappa_{212} \\ \sqrt{2}\kappa_{313} \\ \kappa_{122} \\ \kappa_{133} \\ \kappa_{222} \\ \sqrt{2}\kappa_{121} \\ \sqrt{2}\kappa_{323} \\ \kappa_{211} \\ \kappa_{233} \\ \kappa_{333} \\ \sqrt{2}\kappa_{131} \\ \sqrt{2}\kappa_{232} \\ \kappa_{311} \\ \kappa_{322} \\ \sqrt{2}\kappa_{123} \\ \sqrt{2}\kappa_{231} \\ \sqrt{2}\kappa_{312} \end{pmatrix} \in \mathbb{R}^{18}, \quad \tilde{\mathbb{D}} \in \mathbb{R}^{18 \times 18}. \quad (10)$$

These orderings of coefficients in the matrix-vector notations result in specific block structures of the matrices $\tilde{\mathbb{C}}$ and $\tilde{\mathbb{D}}$, which are visualized in Fig. 1 with their corresponding non-zero entries resulting from the cubic material symmetry. Note that the following relationships between the unique coefficients of $\tilde{\mathbb{C}}$ and \mathbb{C} , as well as $\tilde{\mathbb{D}}$ and \mathbb{D} hold:

$$\begin{aligned} \tilde{C}_{11} &= C_{1111}, \quad \tilde{C}_{12} = C_{1122}, \quad \tilde{C}_{44} = C_{1212}, \\ \tilde{D}_{11} &= D_{111111}, \quad \tilde{D}_{22} = 2D_{212212}, \quad \tilde{D}_{44} = D_{122122}, \quad \tilde{D}_{16,16} = 2D_{123123}, \\ \tilde{D}_{12} &= D_{111212}, \quad \tilde{D}_{14} = \sqrt{2}D_{111122}, \quad \tilde{D}_{23} = 2D_{212313}, \quad \tilde{D}_{24} = \sqrt{2}D_{212122}, \\ \tilde{D}_{25} &= \sqrt{2}D_{212133}, \quad \tilde{D}_{45} = D_{122133}, \quad \tilde{D}_{16,17} = 2D_{123231}. \end{aligned} \quad (11)$$

From variation of the internal work given by the strain energy function and the external work of the linear elastic second gradient continuum (4), the weak form of the balance of linear momentum can be

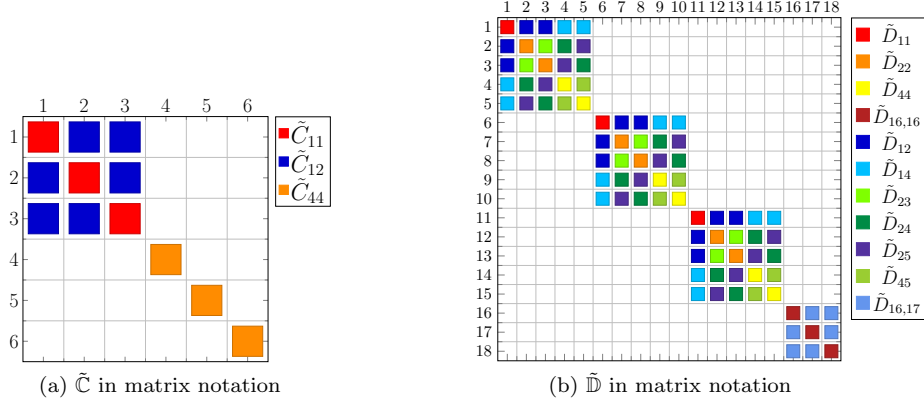


Figure 1: Illustration of the structure of the constitutive tensors $\tilde{\mathbf{C}}$ and $\tilde{\mathbf{D}}$ in matrix notation for microstructures with cubic anisotropy. The colors indicate coefficients with the same value.

derived as:

$$\begin{aligned}
\delta W_{\text{int}} &= \delta W_{\text{ext}} \\
\Leftrightarrow \int_{\Omega} \boldsymbol{\sigma} : \delta \boldsymbol{\varepsilon} + \boldsymbol{\tau} : \delta \boldsymbol{\kappa} dV &= \int_{\Omega} \mathbf{f} \cdot \delta \mathbf{u} dV + \int_{\Gamma_1} \bar{\mathbf{t}}^1 \cdot \delta \mathbf{u} dA + \int_{\Gamma_2} \bar{\mathbf{t}}^2 \cdot \nabla \delta \mathbf{u} \cdot \mathbf{n} dA, \\
\Leftrightarrow \int_{\Omega} \sigma_{ij} \delta \varepsilon_{ij} + \tau_{ijk} \delta \kappa_{ijk} dV &= \int_{\Omega} f_i \delta u_i dV + \int_{\Gamma_1} \bar{t}_i^1 \delta u_i dA + \int_{\Gamma_2} \bar{t}_i^2 \delta u_{i,j} n_j dA.
\end{aligned} \tag{12}$$

Here, $\Gamma_1 \subset \partial\Omega$ and $\Gamma_2 \subset \partial\Omega$ denote the von Neumann boundaries with applied surface tractions $\bar{\mathbf{t}}^1 : \Gamma_1 \rightarrow \mathbb{R}^3$ and double tractions $\bar{\mathbf{t}}^2 : \Gamma_2 \rightarrow \mathbb{R}^3$, respectively, $\mathbf{n} : \Gamma_{1,2} \rightarrow \mathbb{R}^3$ the outer normals on the boundary, and $\mathbf{f} : \Omega \rightarrow \mathbb{R}^3$ external volume loads.

3. Microscale modeling

Having introduced the macroscale modeling approach of lattice structures as linear elastic second gradient continua, we now introduce the microscale modeling concept of representing the unit cells of lattice-metamaterials as beam structures.

3.1. Lattice-metamaterials as 3D beam structures

Cellular structures and metamaterials are characterized by their periodic microstructure, which is generated by repetition of a (non-unique) representative unit cell. For truss-like lattices with slender struts, these unit cells are typically modeled as beam structures, see Fig. 2. To capture the range from very slender to moderately thick strut members, we here use a shear-deformable, Timoshenko-like 3D beam model. In particular, the geometrically exact, nonlinear Cosserat rod or Reissner–Simo beam model is employed [62, 63], but restricted to the infinitesimal deformation regime.

The kinematic configuration of a beam as a framed curve is represented by the arc-length parameterized centerline curve $\mathbf{r}(s) : [0, \ell] \rightarrow \mathbb{R}^3$ and an orthonormal frame (rotation matrix) field $\mathbf{R}(s) : [0, \ell] \rightarrow SO(3)$, which represents the orientation of the cross-sections. The tensile and shear strain vector $\boldsymbol{\varepsilon}_b$ and the bending curvatures and torsional strains $\boldsymbol{\kappa}_b$ are computed as:

$$\boldsymbol{\varepsilon}_b = \mathbf{R}^\top \mathbf{r}' - \mathbf{e}_3, \quad \boldsymbol{\kappa}_b = [\mathbf{R}'^\top \mathbf{R}]_{\times}, \tag{13}$$

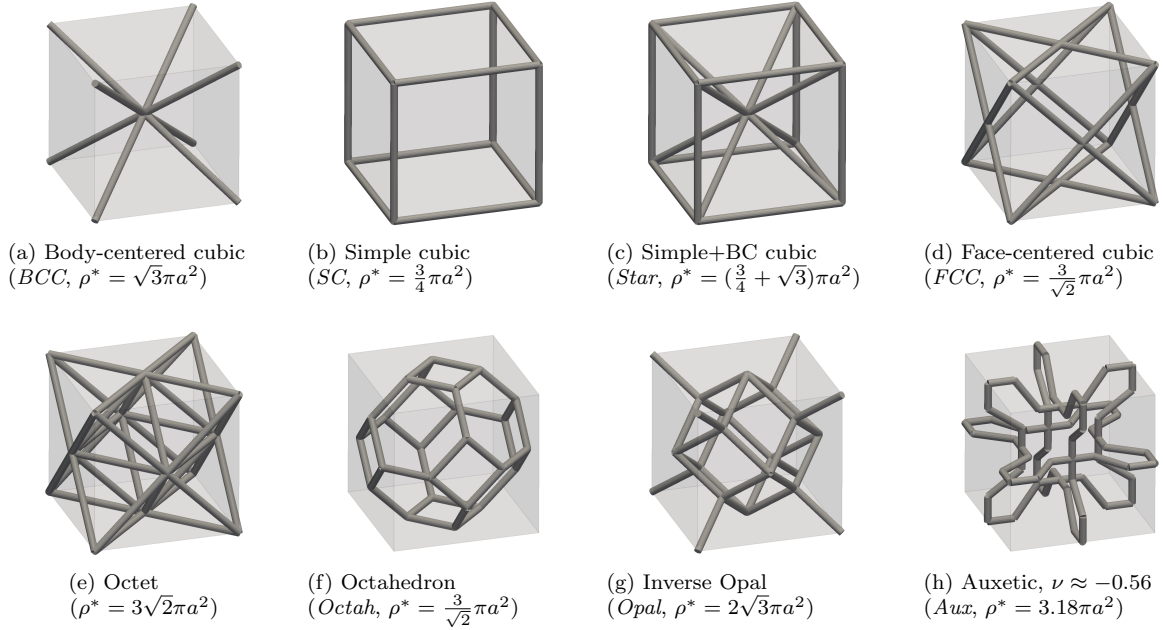


Figure 2: Illustration of the unit cells of the beam-lattice microstructures with cubic symmetry, here with an aspect ratio of $a = d/L = 0.05$, where $d = 2r$ is the strut diameter and L is the size of the cell. Abbreviated names and effective densities ρ^* are given in parenthesis

where \cdot' denotes the arc-length derivative with respect to s , \mathbf{e}_3 the Cartesian basis vector $(0, 0, 1)^\top$, and $[\cdot]_\times$ the generating vector of a skew-symmetric matrix. The subscripts \cdot_b are used to indicate quantities referring to the beam model, in contrast to the symbols used for the macroscopic quantities in Sect. 2.

Using these two strain vectors, the stress resultants are derived by linear elastic constitutive laws:

$$\boldsymbol{\sigma}_b = \mathbf{C}_b \boldsymbol{\varepsilon}_b, \quad \boldsymbol{\chi}_b = \mathbf{D}_b \boldsymbol{\kappa}_b, \quad (14)$$

with the diagonal constitutive matrices:

$$\mathbf{C}_b = \text{diag}\{kG_b A_b, G_b A_b, E_b A_b\}, \quad \mathbf{D}_b = \text{diag}\{E_b I_b, E_b I_b, G_b J_b\}, \quad (15)$$

which are given in terms of the material properties of the beam, the elastic modulus E_b and shear modulus $G_b = E_b/(2 + 2\nu_b)$ with Poisson's ratio ν_b , and the cross-section parameters, area $A_b = \pi r^2$, second moment of area $I_b = \pi r^2/12$, torsion constant $J_b = 2I_b$, and shear correction factor $k = 5/6$, which are given in terms of the radius r (or diameter $d = 2r$) for circular cross-sections. It should be noted here that the microscopic constitutive models (15) are linear in E_b , which allows the normalization of microscopic simulations with respect to E_b later in Sect. 5.

These stress measures are transformed to the material configuration to define the internal force and moment resultants \mathbf{n}_b and \mathbf{m}_b , respectively:

$$\mathbf{n}_b = \mathbf{R} \boldsymbol{\sigma}_b, \quad \mathbf{m}_b = \mathbf{R} \boldsymbol{\chi}_b, \quad (16)$$

Then, the balance equations of linear and angular momentum are formulated:

$$\mathbf{n}_b'(s) = \mathbf{0}, \quad \mathbf{m}_b'(s) + \mathbf{r}'(s) \times \mathbf{n}_b(s) = \mathbf{0}, \quad (17)$$

which have to be fulfilled $\forall s \in (0, \ell)$. The microscopic boundary value problem is completed by boundary conditions for $s = 0, \ell$; either of Dirichlet type given as $\mathbf{r}(s) = \bar{\mathbf{r}}$, $\mathbf{R}(s) = \bar{\mathbf{R}}$, or of Neumann type given as $\mathbf{n}_b(s) = \bar{\mathbf{n}}_b$, $\mathbf{m}_b(s) = \bar{\mathbf{m}}_b$. Here, internally applied external forces and moments are not considered.

The lattice unit cells are beam assemblies or structures consisting of several beams. Here, they are modeled such that interfaces only occur at the ends of individual beams and compatibility conditions are formulated such that the joints are rigid, i.e., deformed centerline positions \mathbf{r} and changes of orientations $\Delta\mathbf{R} = \mathbf{R}\mathbf{R}_0^{-1}$ need to be equal at all beam ends meeting at an interface, and balance of linear and angular momentum must hold, see [59].

However, to accurately reproduce the behavior of physical, e.g., 3D printed, lattice structures, it can be necessary to further increase or reduce the stiffness at the joints. For additively manufactured lattices, it has been observed that polymeric structures with moderately thick struts can require stiffer joints, because of the smoothed and overlapping shape of joints, while metallic lattices may have defects at joints that make them less rigid and softer [4, 7, 22, 23]. These effects are neglected here and the joints are assumed to be perfectly rigid. They could, however, be implemented into the framework without incurring any changes to the homogenization procedure.

3.2. Isogeometric collocation method

For the numerical discretization of the beam model as introduced above, we here employ an isogeometric collocation method. The method is briefly outlined in the following and further details are described in [59]. It should be noted, however, that the general multiscale modeling framework with the homogenization procedure presented below in Sect. 4 could also be realized with any other suitable discretization method applied to the beam model.

The centerline curve \mathbf{r} of a beam is discretized as a spline curve $\mathbf{r}_h : [0, \ell] \rightarrow \mathbb{R}^3$ and the frame \mathbf{R} parameterized by unit quaternions $\mathbf{R} = \mathbf{R}(\mathbf{q})$, $\mathbf{q} \in \mathcal{H} = \{\mathbf{q} \in \mathbb{R}^4, \|\mathbf{q}\| = 1\}$, which are also discretized as a spline curve $\mathbf{q}_h : [0, \ell] \rightarrow \mathbb{R}^4, \|\mathbf{q}_h\| = 1$:

$$\mathbf{r}_h(\xi) = \sum_{i=1}^n N_i(\xi) \mathbf{r}_i, \quad \mathbf{q}_h(\xi) = \sum_{i=1}^n N_i(\xi) \mathbf{q}_i, \quad (18)$$

with univariate spline basis functions N_i and control points $\mathbf{r}_i \in \mathbb{R}^3$ and $\mathbf{q}_i \in \mathbb{R}^4$. Then, a collocation approach is applied to the strong form of the balance equations (17) and the normalization condition for the quaternions, which are evaluated at a set of n collocation points $\tau_j \in [0, \ell]$:

$$\begin{aligned} \mathbf{n}'_b(\mathbf{r}_h, \mathbf{q}_h; \tau_j) &= \mathbf{0}, \\ \mathbf{m}'_b(\mathbf{r}_h, \mathbf{q}_h; \tau_j) + \mathbf{r}'_h(\tau_j) \times \mathbf{n}_b(\mathbf{r}_h, \mathbf{q}_h; \tau_j) &= \mathbf{0}, \\ \|\mathbf{q}_h(\tau_j)\|^2 - 1 &= 0. \end{aligned} \quad (19)$$

The resulting nonlinear system of $7n$ equations is solved to determine the $7n$ unknowns, the centerline and rotation control points \mathbf{r}_i and \mathbf{q}_i , respectively.

This approach has already been applied to the full-scale simulation of 3D lattice structures under large deformations in [7]. Here, it is used to discretize the microscale, i.e., the RUCs of beam-lattice structures and homogenize their mechanical response, as will be outlined below in Sect. 4.

4. Homogenization of the second gradient constitutive models

The general assumption of classical homogenization theory and multiscale simulation is that the displacements, strains and stresses at a point in the macroscopic continuum Ω can be defined as the mean values of the respective quantities with respect to a representative volume element or unit cell Ω_m of the microstructure. For instance, for the strain tensor $\boldsymbol{\varepsilon}$ the average is defined as:

$$\boldsymbol{\varepsilon} = \langle \boldsymbol{\varepsilon}_m \rangle := \frac{1}{|\Omega_m|} \int_{\Omega_m} \boldsymbol{\varepsilon}_m(\mathbf{x}) dV, \quad (20)$$

The connection between microscale and macroscale is then established by the Hill–Mandel condition, which states the equivalence of the macroscopic, second gradient energy potential Ψ , see (4), and the effective potential energy $\Psi_m = W_m/|\Omega_m|$ of the microstructural unit cell [46]:

$$\Psi_m = \Psi \quad \Leftrightarrow \quad \langle \boldsymbol{\sigma}_m : \boldsymbol{\varepsilon}_m \rangle = \boldsymbol{\sigma} : \boldsymbol{\varepsilon} + \boldsymbol{\tau} : \boldsymbol{\kappa}. \quad (21)$$

For a sequential multiscale simulation, this means that an effective macroscopic constitutive model $\boldsymbol{\sigma} = \mathbb{C} : \boldsymbol{\varepsilon}$, $\boldsymbol{\tau} = \mathbb{D} : \boldsymbol{\kappa}$ must be obtained from homogenization of the microstructure, i.e., the coefficients of the effective first-order constitutive tensor \mathbb{C} and the effective second-order constitutive tensor \mathbb{D} are required, see (5). In general, this is achieved by prescribing certain values for the macroscopic strain measures on the unit cell Ω_m , computing the resulting microscopic deformation field, and then averaging the resulting stress measures or internal energy. In the following, a homogenization procedure for computing \mathbb{C} and \mathbb{D} based on modeling of the lattice unit cells as 3D beam structures, see Sect. 3, is derived.

4.1. Micro-macro transition

When the microscopic unit cells are modeled as discrete structures, like it is the case here, volume averages such as the strain average formulated (20) cannot be computed, since there is no microscopic continuum [47]. The same holds when these volume integrals are transformed onto boundary integrals, since the cell boundaries are not manifolds, either. Thus, a more direct relation between the microscopic beam models and the macroscopic second gradient continuum must be established.

For a Timoshenko-type beam, see Sect. 3.1, the internal energy W_b is computed as:

$$W_b = \frac{1}{2} \int_0^\ell \boldsymbol{\varepsilon}_b \cdot \boldsymbol{\sigma}_b + \boldsymbol{\kappa}_b \cdot \boldsymbol{\chi}_b \, ds = \frac{1}{2} \int_0^\ell \boldsymbol{\varepsilon}_b \cdot \boldsymbol{\sigma}_b \, ds + \frac{1}{2} \int_0^\ell \boldsymbol{\kappa}_b \cdot \boldsymbol{\chi}_b \, ds =: W_b^s + W_b^b. \quad (22)$$

Here, W_b^s and W_b^b indicate the stretching (and shearing) and the bending (and torsional) energies of the beam, respectively. If the beam is in an equilibrium configuration, i.e., if a minimum of the total potential energy is assumed, in the absence of external forces and moments the internal energy can be expressed in terms of the external energy as:

$$W_b = \frac{1}{2} [\mathbf{u}_b \cdot \mathbf{n}_b + \boldsymbol{\phi}_b \cdot \mathbf{m}_b]_0^\ell, \quad (23)$$

where $\mathbf{u}_b, \boldsymbol{\phi}_b, \mathbf{n}_b, \mathbf{m}_b \in \mathbb{R}^3$ are the centerline displacements, change of rotations, normal forces, and moments at the beam ends $s = 0, \ell$. Thus, the effective energy potential $\Psi_m = W_m/|\Omega_m|$ of the microstructural assembly with n beams can be expressed as:

$$2\Psi_m |\Omega_m| = 2W_m = 2 \sum_{i=1}^n W_b^i = \sum_{i=1}^n [\mathbf{u}_b^i \cdot \mathbf{n}_b^i + \boldsymbol{\phi}_b^i \cdot \mathbf{m}_b^i]_0^{\ell^i} = \sum_{j=1}^c \mathbf{u}_b^j \cdot \mathbf{n}_b^j + \boldsymbol{\phi}_b^j \cdot \mathbf{m}_b^j, \quad (24)$$

where the superscripts \cdot^i refer to the i -th beam and the superscripts \cdot^j refer directly to the c beam ends/nodes located on the boundary of the unit cell, since equilibrium of forces and moments must hold at internal joints with rigid connections, see Sect. 3.1.

We proceed by prescribing a quadratic displacement field for the centerline positions $\mathbf{r} = \mathbf{r}_0 + \mathbf{u}$ of all boundary nodes:

$$\mathbf{u}(\mathbf{x}) = \boldsymbol{\varepsilon}^* \cdot \mathbf{x} + \frac{1}{2} (\boldsymbol{\kappa}^* \cdot \mathbf{x}) \cdot \mathbf{x} + \mathbf{w}(\mathbf{x}), \quad u_i = \varepsilon_{ij}^* x_j + \frac{1}{2} \kappa_{ijk}^* x_j x_k + w_i, \quad (25)$$

where $\boldsymbol{\varepsilon}^* \in \mathbb{R}^{3 \times 3}$ with $\varepsilon_{ij}^* = \varepsilon_{ji}^*$, $\boldsymbol{\kappa}^* \in \mathbb{R}^{3 \times 3 \times 3}$ with $\kappa_{ijk}^* = \kappa_{ikj}^*$, $\mathbf{w} \in \mathbb{R}^3$ is a fluctuation vector field, and $\mathbf{x} \equiv \mathbf{r}_0$ is the initial centerline position of the node, i.e., the beam end-point on the boundary. Furthermore, a linear ansatz is made for the change of the rotations at boundary nodes:

$$\boldsymbol{\phi}(\mathbf{x}) = \text{axl}(\mathbf{R}_{\boldsymbol{\kappa}^*}(\mathbf{x})) + \boldsymbol{\psi}(\mathbf{x}) = -\frac{1}{2} \boldsymbol{\varepsilon} : \boldsymbol{\kappa}^* \cdot \mathbf{x} + \boldsymbol{\psi}(\mathbf{x}), \quad \phi_i = -\frac{1}{2} \varepsilon_{ilm} \kappa_{lmj}^* x_j + \psi_i, \quad (26)$$

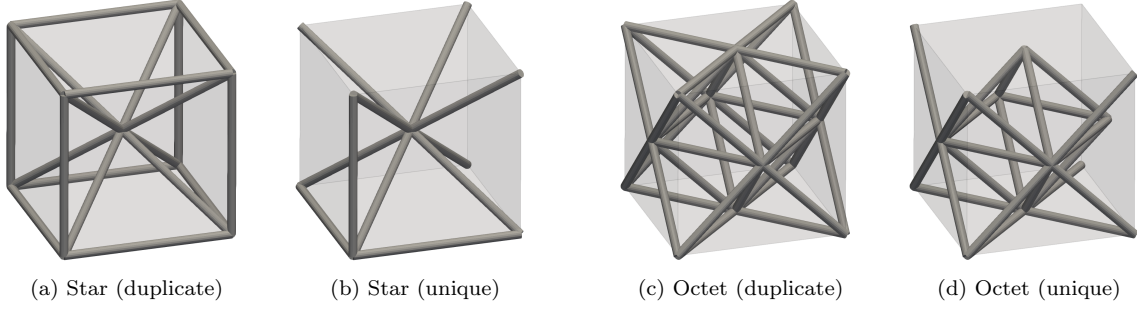


Figure 3: Unit cells of Star and Octet lattices with and without duplicate struts

where $\boldsymbol{\psi} \in \mathbb{R}^3$ is again a fluctuation field and:

$$\mathbf{R}_{\boldsymbol{\kappa}}(\mathbf{x}) = \mathbf{I} + \frac{1}{2} (\nabla \mathbf{u}(\mathbf{x}) - \nabla \mathbf{u}(\mathbf{x})^\top) = \mathbf{I} + \frac{1}{2} (\boldsymbol{\kappa}^* \cdot \mathbf{x} - (\boldsymbol{\kappa}^* \cdot \mathbf{x})^\top), \quad (27)$$

is the rotation part of the infinitesimal strain tensor implied by (25), with $\text{axl}(\mathbf{R}_{\boldsymbol{\kappa}^*}(\mathbf{x}))$ being its axial vector, which can be conveniently expressed using the third-order Levi–Civita permutation tensor $\boldsymbol{\epsilon}$.

Substitution of (25) and into (24) then yields, dropping the summation over all c boundary nodes as well as the superscripts $\cdot j$ for clarity and using only index notation:

$$\begin{aligned} u_i n_i + \phi_i m_i &= (\varepsilon_{ij}^* x_j + \frac{1}{2} \kappa_{ijk}^* x_j x_k + w_i) n_i + (-\frac{1}{2} \epsilon_{ilm} \kappa_{lmj}^* x_j + \psi_i) m_i \\ &= \varepsilon_{ij}^* n_i x_j + \frac{1}{2} \kappa_{ijk}^* (n_i x_j x_k - \epsilon_{ijl} m_l x_k) + n_i w_i + \psi_i m_i \\ &= \varepsilon_{ij}^* \sigma_{ij}^* + \kappa_{ijk}^* (\hat{\tau}_{ijk}^* - \epsilon_{ijl} \mu_{lk}^*) + n_i w_i + \psi_i m_i. \end{aligned} \quad (28)$$

Here, the microscopic stress tensor can be identified as $\sigma_{ij}^* = n_i x_j$, the force-induced hyperstress tensor as $\hat{\tau}_{ijk}^* = \frac{1}{2} n_i x_j x_k$, and the moment tensor as $\mu_{lk}^* = \frac{1}{2} m_l x_k$, the latter two being generally non-symmetric. However, without loss of generality [61], a symmetric microscopic hyperstress tensor can be introduced as:

$$\tau_{ijk}^* = \frac{1}{2} (\hat{\tau}_{ijk}^* + \hat{\tau}_{ikj}^* - \epsilon_{ijl} \mu_{lk}^* - \epsilon_{ikl} \mu_{lj}^*) = \frac{1}{4} (n_i x_j x_k + n_i x_k x_j - \epsilon_{ijl} m_l x_k - \epsilon_{ikl} m_l x_j). \quad (29)$$

Now, the macroscopic quantities in the Hill–Mandel condition (21) can be identified with their microscopic counterparts in the beam model:

$$\sigma_{ij} \varepsilon_{ij} + \tau_{ijk} \kappa_{ijk} \quad \Leftrightarrow \quad \frac{1}{|\Omega_m|} (\sigma_{ij}^* \varepsilon_{ij}^* + \tau_{ijk}^* \kappa_{ijk}^* + n_i w_i + m_i \psi_i). \quad (30)$$

This shows that the microscopic prescribed strain tensors and the resulting stress tensors can be regarded as effective strain and stress tensors of the macroscopic second gradient model:

$$\boldsymbol{\varepsilon}_m = \boldsymbol{\varepsilon}^*, \quad \boldsymbol{\kappa}_m = \boldsymbol{\kappa}^*, \quad \boldsymbol{\sigma}_m = \frac{1}{|\Omega_m|} \boldsymbol{\sigma}^*, \quad \boldsymbol{\tau}_m = \frac{1}{|\Omega_m|} \boldsymbol{\tau}^*. \quad (31)$$

While the strain tensors $\boldsymbol{\varepsilon}_m, \boldsymbol{\kappa}_m$ are prescribed as boundary conditions for displacements and rotations of the boundary nodes of the unit cell, the stress tensors $\boldsymbol{\sigma}_m, \boldsymbol{\tau}_m$ can be computed by solving the boundary value problem of the microscopic unit cell and obtaining the resulting forces \mathbf{n} and moments \mathbf{m} . This requires the summation of respective contributions from all boundary nodes, which we have dropped in the notation of (25)–(30). If a RUC model with duplicate struts is used, see Fig. 3, the contributions from struts on edges and faces have to be weighted with factors 0.25 and 0.5, respectively.

4.2. Boundary conditions

The micro-macro-transition in (30) only fulfills the Hill–Mandel condition if the work contributions of the fluctuations \mathbf{w} and $\boldsymbol{\psi}$ vanish (summed over all c boundary nodes \mathbf{x}^j):

$$\sum_{j=1}^c \mathbf{w}^j \cdot \mathbf{n}^j + \boldsymbol{\psi}^j \cdot \mathbf{m}^j. \quad (32)$$

This has to be ensured by the choice of kinematic boundary conditions.

Obviously, affine displacement boundary conditions with $\mathbf{w} \equiv \mathbf{0}$ and $\boldsymbol{\psi} \equiv \mathbf{0}$ are a suitable choice, which is however well known to over-estimate the effective stiffness. Periodic boundary conditions are also applicable, in which $\mathbf{w}(\mathbf{x}^+) = \mathbf{w}(\mathbf{x}^-)$ and $\boldsymbol{\psi}(\mathbf{x}^+) = \boldsymbol{\psi}(\mathbf{x}^-)$, as well as $\mathbf{n}(\mathbf{x}^+) = -\mathbf{n}(\mathbf{x}^-)$ and $\mathbf{m}(\mathbf{x}^+) = -\mathbf{m}(\mathbf{x}^-)$ must hold for each pair of nodes $(\mathbf{x}^+, \mathbf{x}^-)$ on opposing boundaries. Also anti-periodic fluctuations would be admissible (at least on some part of the boundary), see [46, 64, 65], i.e., $\mathbf{w}(\mathbf{x}^+) = -\mathbf{w}(\mathbf{x}^-)$ and $\boldsymbol{\psi}(\mathbf{x}^+) = -\boldsymbol{\psi}(\mathbf{x}^-)$, as well as $\mathbf{n}(\mathbf{x}^+) = \mathbf{n}(\mathbf{x}^-)$ and $\mathbf{m}(\mathbf{x}^+) = \mathbf{m}(\mathbf{x}^-)$. Furthermore, free boundary conditions would also be possible, where $\mathbf{n} \equiv \mathbf{0}$ and $\mathbf{m} \equiv \mathbf{0}$, yielding arbitrary values for \mathbf{w} and $\boldsymbol{\psi}$, and thus also \mathbf{u} and $\boldsymbol{\phi}$. However, since the macroscopic strain tensors $\boldsymbol{\varepsilon}^*$, $\boldsymbol{\kappa}^*$ are to be enforced, see (25), but cannot be explicitly computed as microscopic averages, the latter two choices of anti-periodic and free boundary conditions appear less reasonable.

Since rigid body motions must be restricted due to numerical reasons, we typically apply affine boundary conditions for the displacements of the nodes located in the corners of the unit cell. If no nodes are located in corners, like for Octahedron and Auxetic unit cells, other suitable points are identified. In addition to that, we will numerically investigate the effect of different types and combinations of boundary conditions for displacements and rotations.

4.3. Determination of the constitutive tensors

Assuming that the boundary conditions are chosen such that the fluctuations do not contribute any work, the Hill–Mandel condition for the second gradient continuum holds and the macroscopic strain and stress tensors can be identified with their microscopic counterparts, i.e., the prescribed strain tensors and the effective stress tensors, see (30) and (31):

$$\Psi = \Psi_m \quad \Leftrightarrow \quad \frac{1}{2}(\boldsymbol{\sigma} : \boldsymbol{\varepsilon} + \boldsymbol{\tau} \dot{ : } \boldsymbol{\kappa}) = \frac{1}{2}(\boldsymbol{\sigma}_m : \boldsymbol{\varepsilon}_m + \boldsymbol{\tau}_m \dot{ : } \boldsymbol{\kappa}_m). \quad (33)$$

Note that prescribing $\boldsymbol{\varepsilon}_m = \boldsymbol{\varepsilon}^*$ and $\boldsymbol{\kappa}_m = \boldsymbol{\kappa}^*$ as boundary conditions (in whatever way), does not guarantee that $\boldsymbol{\varepsilon}_m, \boldsymbol{\kappa}_m$ represent the volume averages of the strains as defined in (20), since there is no microscopic continuum over which the strains could be integrated to evaluate such averages. However, the equivalence can be verified numerically by showing that (33) holds, i.e., by computing $\boldsymbol{\sigma}_m$ and $\boldsymbol{\tau}_m$ for given $\boldsymbol{\varepsilon}_m$ and $\boldsymbol{\kappa}_m$, and then checking the macroscopic, effective energy against the microscopic internal energy W_m for the beam structure, see (24):

$$\frac{2W_m}{|\Omega_m|} = 2\Psi_m \stackrel{!}{=} \boldsymbol{\sigma}_m : \boldsymbol{\varepsilon}_m + \boldsymbol{\tau}_m \dot{ : } \boldsymbol{\kappa}_m. \quad (34)$$

Now, the coefficients of the classical, first-order effective constitutive tensor in $\boldsymbol{\sigma} = \mathbb{C} : \boldsymbol{\varepsilon}$, see (5), can simply be identified by prescribing a single non-zero microscopic strain component $\varepsilon_{kl} \neq 0$, solving the BVP of the unit cell, evaluating the resulting $\boldsymbol{\sigma}_m$, and assigning the corresponding coefficients as $C_{ijkl} = \sigma_{ij}/\varepsilon_{kl}$.

Likewise, the coefficients of the second-gradient effective constitutive tensor in $\boldsymbol{\tau} = \mathbb{D} \dot{ : } \boldsymbol{\kappa}$, see (5), can be identified by setting only a single $\kappa_{lmn} \neq 0$ and computing $D_{ijklmn} = \tau_{ijk}/\kappa_{lmn}$.

In this process, the material symmetries of the unit cell and its resulting effective behavior can be exploited, see Sect. 5. Thus, for a lattice with cubic anisotropy, the 3 unique coefficients $C_{1111}, C_{1122}, C_{1212}$ can be computed using only 2 simulations and the 11 unique coefficients of \mathbb{D} using 6 further ones, which becomes obvious from the structure of $\tilde{\mathbb{C}}, \tilde{\mathbb{D}}$ as shown in Fig. 1. The classical coefficients $\tilde{C}_{11} = C_{1111}, \tilde{C}_{12} =$

$C_{1122}, \tilde{C}_{44} = C_{1212}$ can also be formulated in terms of a macroscopic, effective Young's modulus E , Poisson's ratio ν and shear modulus G (which is independent of E and ν):

$$G = \tilde{C}_{44}, \quad \nu = \frac{\tilde{C}_{12}}{\tilde{C}_{11} + \tilde{C}_{12}}, \quad E = \frac{\tilde{C}_{12}(1 + \nu)(1 - 2\nu)}{\nu}. \quad (35)$$

Furthermore, for non-centro-symmetric unit cells the same strategy can be applied and the coefficients of the coupling tensor \mathbb{M} of (4) can be computed as $M_{ijklmn} = \sigma_{ij}/\kappa_{lmn}$ when only $\kappa_{lmn} \neq 0$.

5. Results and discussion

In the following, the homogenization results for the effective constitutive tensors \mathbb{C} and \mathbb{D} are obtained for the 8 types of lattice micro-architectures shown in Fig. 2. Analytical values for the relative densities ρ^* of the different lattice types, which are defined as the volume of the beam structure over the total volume of the RUC $|\Omega_m| = L^3$, but here neglect overlaps between the struts or fillets at the joints, are also provided in the figure. Those are typically relevant in practical applications, where a trade-off between weight of the structure and its mechanical stiffness is sought.

For the following analyses, all quantities are regarded as unitless, but could be taken as mm for lengths and MPa for stresses and Young's moduli. Since the Young's modulus of the material of the microstructure is a linear parameter in the elastic beam theory used to model the microstructures, see (15), the effective constitutive tensors \mathbb{C} and \mathbb{D} resulting from homogenization, as well as the effective, macroscopic moduli E and G , depend linearly on E_b . Thus, $E_b = 1$ is used here so that the coefficients for any material can simply be obtained by multiplication with the actual Young's modulus E_b . The Poisson's ratio of the beam material is chosen as $\nu_b = 0.33$.

For the isogeometric discretization, $p = 8, n = 24$ is used, which yields a sufficiently high numerical accuracy of the numerical results, see [59], which are computed here with double precision. For the microscale simulations, strains and second gradients are prescribed with a perturbation of $\epsilon = 10^{-5}$, see Sect. 4, such that the deformations and strains of the nonlinear beam model can be assumed as infinitesimal. Of course, the obtained linear elastic models can be applied within the typical range of validity of linear elasticity.

5.1. Verification of the homogenization approach

First, a verification of the proposed homogenization approach and its implementation is carried out. The objectives are to confirm that the chosen boundary conditions fulfill the Hill–Mandel condition (33), i.e., that the fluctuations do not contribute any work, see (32), and to show that they yield deformed states equivalent to those expected in an infinitely periodic microstructure. Using a cell length of $L = 10$ and an aspect ratio of $a = 0.05$ ($r = 0.25$), “infinite” lattices are simulated by lattice structures consisting of $5 \times 5 \times 5$, $7 \times 7 \times 7$, or $9 \times 9 \times 9$ unit cells, for which displacements are prescribed according to the given second gradient κ_m at all repeated unit cell corner nodes, but no rotations are prescribed at any nodes at all. Then, the resulting effective stress σ^* and hyperstress τ^* tensors, as well as internal energy W_m of the beam assembly are computed only for the beams constituting the center cell of the structure. These values are compared against the ones obtained for a single unit cell, for which the displacements are prescribed according to κ_m at all corner nodes. For the BCC, SC and Star cells, which have no other nodes located on the cell boundary, the rotation boundary conditions are chosen either as free, periodic or fully prescribed according to κ_m . Figure 4 shows the resulting deformations of the body-centered cubic (BCC) and simple cubic (SC) unit cells in three scenarios where only $\kappa_{111}, \kappa_{122}$, or κ_{112} are prescribed. In the case of only $\tilde{\kappa}_1 = \kappa_{111} = \epsilon \neq 0$, it is:

$$\mathbf{u}(\mathbf{x}) = \begin{pmatrix} \frac{1}{2}\epsilon x_1^2 \\ 0 \\ 0 \end{pmatrix}, \quad \nabla \mathbf{u}(\mathbf{x}) = \begin{pmatrix} \epsilon x_1 & 0 & 0 \\ 0 & 0 & 0 \\ 0 & 0 & 0 \end{pmatrix}, \quad \mathbf{R}_\kappa(\mathbf{x}) = \begin{pmatrix} 1 & 0 & 0 \\ 0 & 1 & 0 \\ 0 & 0 & 1 \end{pmatrix}, \quad (36)$$

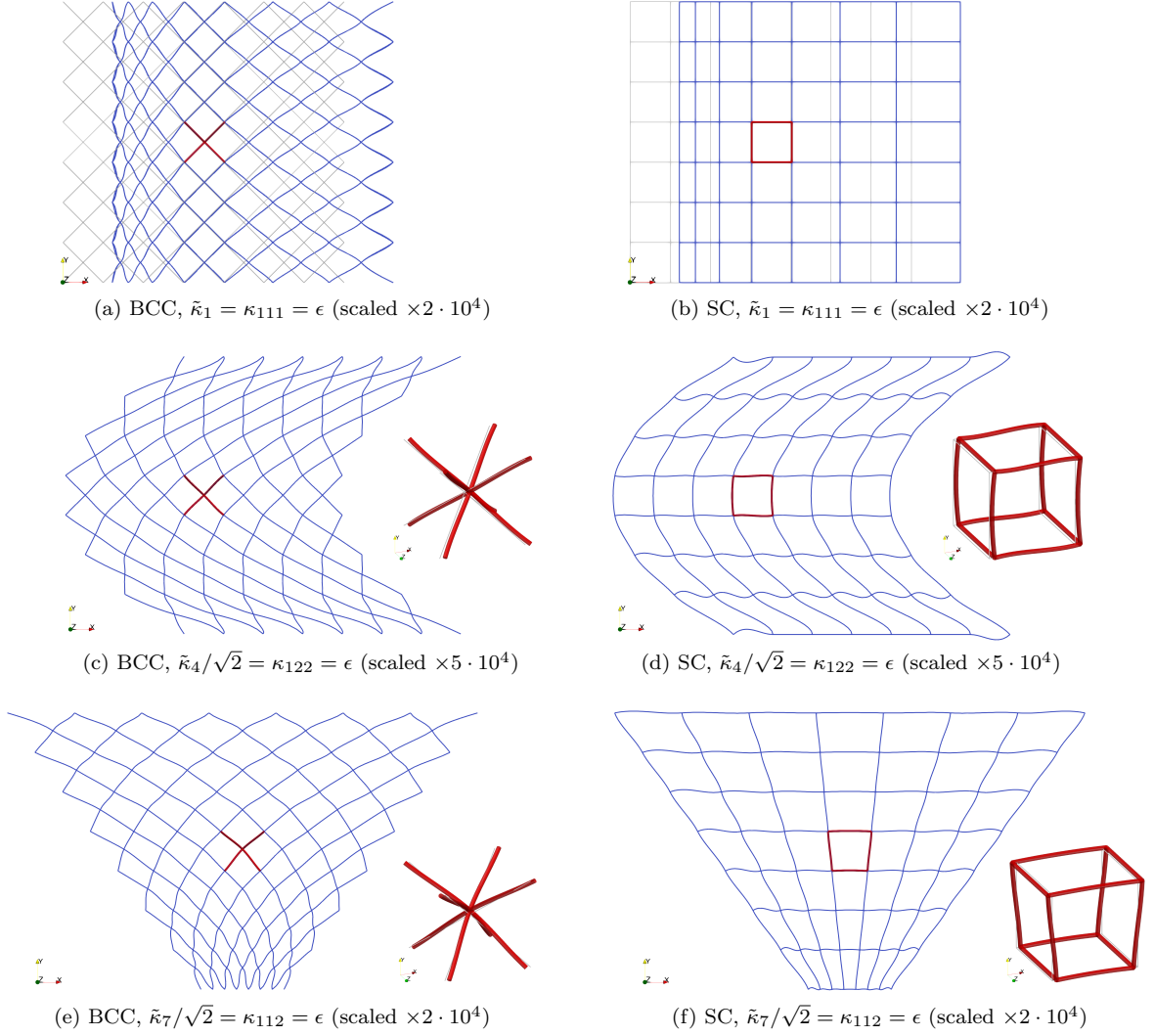


Figure 4: Verification of boundary conditions by a comparison of full-scale simulations of lattices with $7 \times 7 \times 7$ cells (centerlines in blue) against single unit cells with PBC (in red); all projected onto the x_1x_2 -plane, single cell also shown in 3D view; deformations are scaled for better visibility

yielding $\phi(\mathbf{x}) = (0 \ 0 \ 0)^\top$. For $\tilde{\kappa}_4/\sqrt{2} = \kappa_{122} = \epsilon \neq 0$, it is:

$$\mathbf{u}(\mathbf{x}) = \begin{pmatrix} \frac{1}{2}\epsilon x_2^2 \\ 0 \\ 0 \end{pmatrix}, \quad \nabla \mathbf{u}(\mathbf{x}) = \begin{pmatrix} 0 & \epsilon x_2 & 0 \\ 0 & 0 & 0 \\ 0 & 0 & 0 \end{pmatrix}, \quad \mathbf{R}_\kappa(\mathbf{x}) = \begin{pmatrix} 1 & \frac{1}{2}\epsilon x_2 & 0 \\ -\frac{1}{2}\epsilon x_2 & 1 & 0 \\ 0 & 0 & 1 \end{pmatrix}, \quad (37)$$

yielding $\phi(\mathbf{x}) = (0 \ 0 \ -\frac{1}{2}\epsilon x_2)^\top$. For $\tilde{\kappa}_7/\sqrt{2} = \kappa_{112} = \epsilon$, it is:

$$\mathbf{u}(\mathbf{x}) = \begin{pmatrix} \epsilon x_1 x_2 \\ 0 \\ 0 \end{pmatrix}, \quad \nabla \mathbf{u}(\mathbf{x}) = \begin{pmatrix} \epsilon x_2 & \epsilon x_1 & 0 \\ 0 & 0 & 0 \\ 0 & 0 & 0 \end{pmatrix}, \quad \mathbf{R}_\kappa(\mathbf{x}) = \begin{pmatrix} 1 & \frac{1}{2}\epsilon x_1 & 0 \\ -\frac{1}{2}\epsilon x_1 & 1 & 0 \\ 0 & 0 & 1 \end{pmatrix}, \quad (38)$$

yielding, $\phi(\mathbf{x}) = (0 \ 0 \ -\frac{1}{2}\epsilon x_1)^\top$.

Type	RBC / size	κ_{212}	κ_{122}	κ_{123}	$\kappa_{212}, \kappa_{313}$	$\kappa_{212}, \kappa_{122}$	$\kappa_{212}, \kappa_{133}$	$\kappa_{122}, \kappa_{133}$	$\kappa_{123}, \kappa_{123}$
BCC	free	$7.064 \cdot 10^{-5}$	$1.046 \cdot 10^{-13}$	$1.892 \cdot 10^{-2}$	$2.119 \cdot 10^{-4}$	$7.064 \cdot 10^{-5}$	$7.064 \cdot 10^{-5}$	$-1.810 \cdot 10^{-13}$	$7.560 \cdot 10^{-2}$
BCC	periodic	$1.657 \cdot 10^{-4}$	$2.563 \cdot 10^{-5}$	$1.892 \cdot 10^{-2}$	$4.898 \cdot 10^{-4}$	$2.801 \cdot 10^{-4}$	$2.422 \cdot 10^{-4}$	$7.017 \cdot 10^{-5}$	$7.560 \cdot 10^{-2}$
BCC	fixed	$1.657 \cdot 10^{-4}$	$2.563 \cdot 10^{-5}$	$1.892 \cdot 10^{-2}$	$4.898 \cdot 10^{-4}$	$2.801 \cdot 10^{-4}$	$2.422 \cdot 10^{-4}$	$7.017 \cdot 10^{-5}$	$7.560 \cdot 10^{-2}$
BCC	$5 \times 5 \times 5$	$1.657 \cdot 10^{-4}$	$2.563 \cdot 10^{-5}$	$1.892 \cdot 10^{-2}$	$4.897 \cdot 10^{-4}$	$2.801 \cdot 10^{-4}$	$2.421 \cdot 10^{-4}$	$7.018 \cdot 10^{-5}$	$7.560 \cdot 10^{-2}$
BCC	$7 \times 7 \times 7$	$1.657 \cdot 10^{-4}$	$2.563 \cdot 10^{-5}$	$1.892 \cdot 10^{-2}$	$4.898 \cdot 10^{-4}$	$2.801 \cdot 10^{-4}$	$2.422 \cdot 10^{-4}$	$7.017 \cdot 10^{-5}$	$7.560 \cdot 10^{-2}$
BCC	$9 \times 9 \times 9$	$1.657 \cdot 10^{-4}$	$2.563 \cdot 10^{-5}$	$1.892 \cdot 10^{-2}$	$4.898 \cdot 10^{-4}$	$2.801 \cdot 10^{-4}$	$2.422 \cdot 10^{-4}$	$7.017 \cdot 10^{-5}$	$7.560 \cdot 10^{-2}$
SC	free	$2.456 \cdot 10^{-2}$	$2.494 \cdot 10^{-13}$	$5.087 \cdot 10^{-5}$	$4.911 \cdot 10^{-2}$	$2.456 \cdot 10^{-2}$	$2.456 \cdot 10^{-2}$	$7.797 \cdot 10^{-14}$	$1.424 \cdot 10^{-4}$
SC	periodic	$2.456 \cdot 10^{-2}$	$1.527 \cdot 10^{-5}$	$5.151 \cdot 10^{-5}$	$4.912 \cdot 10^{-2}$	$2.459 \cdot 10^{-2}$	$2.457 \cdot 10^{-2}$	$3.054 \cdot 10^{-5}$	$1.430 \cdot 10^{-4}$
SC	fixed	$2.456 \cdot 10^{-2}$	$1.527 \cdot 10^{-5}$	$5.151 \cdot 10^{-5}$	$4.912 \cdot 10^{-2}$	$2.459 \cdot 10^{-2}$	$2.457 \cdot 10^{-2}$	$3.054 \cdot 10^{-5}$	$1.430 \cdot 10^{-4}$
SC	$5 \times 5 \times 5$	$2.456 \cdot 10^{-2}$	$1.453 \cdot 10^{-5}$	$5.151 \cdot 10^{-5}$	$4.912 \cdot 10^{-2}$	$2.459 \cdot 10^{-2}$	$2.457 \cdot 10^{-2}$	$2.907 \cdot 10^{-5}$	$1.430 \cdot 10^{-4}$
SC	$7 \times 7 \times 7$	$2.456 \cdot 10^{-2}$	$1.537 \cdot 10^{-5}$	$5.151 \cdot 10^{-5}$	$4.912 \cdot 10^{-2}$	$2.459 \cdot 10^{-2}$	$2.457 \cdot 10^{-2}$	$3.073 \cdot 10^{-5}$	$1.430 \cdot 10^{-4}$
SC	$9 \times 9 \times 9$	$2.456 \cdot 10^{-2}$	$1.526 \cdot 10^{-5}$	$5.151 \cdot 10^{-5}$	$4.912 \cdot 10^{-2}$	$2.459 \cdot 10^{-2}$	$2.457 \cdot 10^{-2}$	$3.052 \cdot 10^{-5}$	$1.430 \cdot 10^{-4}$
Star	free	$2.464 \cdot 10^{-2}$	$1.355 \cdot 10^{-13}$	$1.897 \cdot 10^{-2}$	$4.937 \cdot 10^{-2}$	$2.464 \cdot 10^{-2}$	$2.464 \cdot 10^{-2}$	$-9.123 \cdot 10^{-14}$	$7.574 \cdot 10^{-2}$
Star	periodic	$2.472 \cdot 10^{-2}$	$4.090 \cdot 10^{-5}$	$1.897 \cdot 10^{-2}$	$4.961 \cdot 10^{-2}$	$2.487 \cdot 10^{-2}$	$2.482 \cdot 10^{-2}$	$1.007 \cdot 10^{-4}$	$7.574 \cdot 10^{-2}$
Star	fixed	$2.472 \cdot 10^{-2}$	$4.090 \cdot 10^{-5}$	$1.897 \cdot 10^{-2}$	$4.961 \cdot 10^{-2}$	$2.487 \cdot 10^{-2}$	$2.482 \cdot 10^{-2}$	$1.007 \cdot 10^{-4}$	$7.574 \cdot 10^{-2}$
Star	$5 \times 5 \times 5$	$2.472 \cdot 10^{-5}$	$4.082 \cdot 10^{-8}$	$1.897 \cdot 10^{-5}$	$4.961 \cdot 10^{-5}$	$2.487 \cdot 10^{-5}$	$2.482 \cdot 10^{-5}$	$1.005 \cdot 10^{-7}$	$7.574 \cdot 10^{-5}$
Star	$7 \times 7 \times 7$	$2.472 \cdot 10^{-5}$	$4.091 \cdot 10^{-8}$	$1.897 \cdot 10^{-5}$	$4.961 \cdot 10^{-5}$	$2.487 \cdot 10^{-5}$	$2.482 \cdot 10^{-5}$	$1.007 \cdot 10^{-7}$	$7.574 \cdot 10^{-5}$
Star	$9 \times 9 \times 9$	$2.472 \cdot 10^{-5}$	$4.090 \cdot 10^{-8}$	$1.897 \cdot 10^{-5}$	$4.961 \cdot 10^{-5}$	$2.487 \cdot 10^{-5}$	$2.482 \cdot 10^{-5}$	$1.007 \cdot 10^{-7}$	$7.574 \cdot 10^{-5}$

Table 1: Comparison of strain energies of body-centered cubic (BCC), simple cubic (SC) and Star cells with $L = 10$, $a = 0.05$ obtained from homogenization of a single unit cell with “free”, “periodic” or “fixed” rotation boundary conditions, or from a lattice with $5 \times 5 \times 5$, $7 \times 7 \times 7$ or $9 \times 9 \times 9$ cells subject to prescribed cell displacements

First of all, it could be observed that the simulations where only $\kappa_{111} \neq 0$ is prescribed yield energy free rigid body motions for any type of cell using periodic displacement boundary conditions, see Fig. 4a and 4b for BCC and SC, respectively. Thus, $\bar{D}_{11}, \bar{D}_{12}, \bar{D}_{14}$ are all 0 and not explicitly provided in any of the following data. The same phenomenon was also observed in [42], but not explicitly discussed there.

In Tab. 1, the resulting effective strain energy density values Ψ_m/ϵ^2 are summarized for the BCC, SC and Star unit cell types for the 3 choices of rotation boundary conditions (RBC), as well as the 3 full-scale structure sizes. As can be seen, the full-scale simulations converge with increasing number of cells and the RUC simulations for both periodic and fixed RBC attain the same values, while the values for free RBC differ. Nevertheless, the Hill–Mandel condition (33) is fulfilled also for free RBC and the energy of the beam structure is equal to the energy that can be computed from the prescribed κ_m and the computed τ_m , see (34).

However, for the other RUC types to be investigated, which – in contrast to BCC, SC and Star – possess struts and nodes on the boundary edges and faces of the RUC, see Fig. 2, the full-scale simulations with prescribed displacements on the cell corner nodes do not necessarily converge and even if they do, the resulting hyperstresses τ_m are not consistent with the prescribed κ_m . Thus, in these cases, the equivalence of the RUC simulations with full-scale simulations cannot be verified, since unlike in [46] the effective strain and second gradient tensors cannot be computed for a beam microstructure. Nevertheless, it could be verified that the Hill–Mandel condition (33) is fulfilled for the RUC simulations for any admissible choice of boundary conditions, i.e., free, periodic, anti-periodic, or fixed. This verifies the derived numerical homogenization framework and allows us to proceed with the evaluation of the constitutive coefficients for the second-gradient constitutive models, for which we will use periodic boundary conditions.

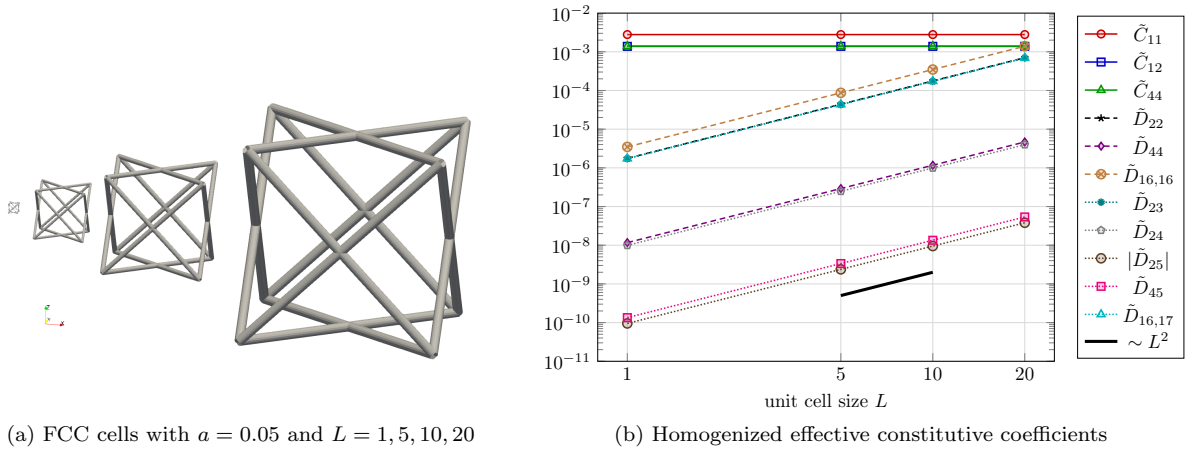


Figure 5: Investigation of the size-dependence of the effective constitutive coefficients of FCC unit cells with constant aspect ratio $a = 0.05$, but varying cell size L

5.2. Size-dependence of constitutive tensors

While the effective first-order constitutive tensor \mathbb{C} is well-known to be independent of the size of the microstructure, the second-order constitutive tensor \mathbb{D} , which relates second gradients to hyperstresses, has been observed to take into account size effects – which is the main motivation behind this work. It should be expected to scale as $\mathbb{D} \sim L^2$, see e.g. [41], where L is in general the characteristic size of the microstructure, i.e., here the edge length of the cubic unit cell L .

To validate this scaling behavior, Fig. 5 shows the homogenization of four FCC unit cells with the same aspect ratio $a = 2r/L = 0.05$, but varying cell sizes of $L = 1, 5, 10, 20$, i.e., beam radii $r = 0.025, 0.125, 0.25, 0.5$. Figure 5b clearly demonstrates that the coefficients of \mathbb{C} are independent of the cell size, while the effective coefficients of \mathbb{D} depend on the cell size as $\mathbb{D} \sim L^2$. It should be noted here that \tilde{D}_{25} is negative and thus $|\tilde{D}_{25}|$ is plotted. Nevertheless, it holds also $\tilde{D}_{25} \sim L^2$ and it has been verified that the tensor \mathbb{D} is positive semi-definite.

Due to the size-dependence of the effective second-order coefficients, we introduce and in the following always compute a normalized second-order constitutive tensor:

$$\bar{\mathbb{D}} = \mathbb{D}/L^2, \quad (39)$$

which can be used to obtain the actual \mathbb{D} for any given unit cell size L .

5.3. Homogenization results and scaling with a

It has also been observed that the dependence of the effective moduli on the aspect ratio of the microstructure, $a = d/L = 2r/L$, or on its relative density ρ^* , which is the volume occupied by material within the unit cell divided by the overall volume of the unit cell, $|\Omega_m| = L^3$, can be represented in terms of scaling laws. The classical polynomial scaling laws for beam-like lattices have been presented by Gibson and Ashby [10, 11]:

$$\rho^* \sim a^2, \quad E \sim \rho^{*\gamma} \sim a^{2\gamma}, \quad (40)$$

where $\gamma \approx 1$ for stretch-dominated and $\gamma \approx 2$ for bending-dominated micro-architectures. An extension of this model was introduced in [23]:

$$E = c_1 a^\alpha + c_2 a^\beta, \quad (41)$$

where the exponents were found to be $\alpha \approx 2$ and $\beta \approx 4$ for stretch-dominated and $\alpha \approx 4$ and $\beta \approx 6$ for bending-dominated microstructures. As an (overly) simple explanation for these scaling laws, it can be noted that the cross-section area and thus the tensional stiffness of a beam scales as $E_b A_b \sim d^2$, while the

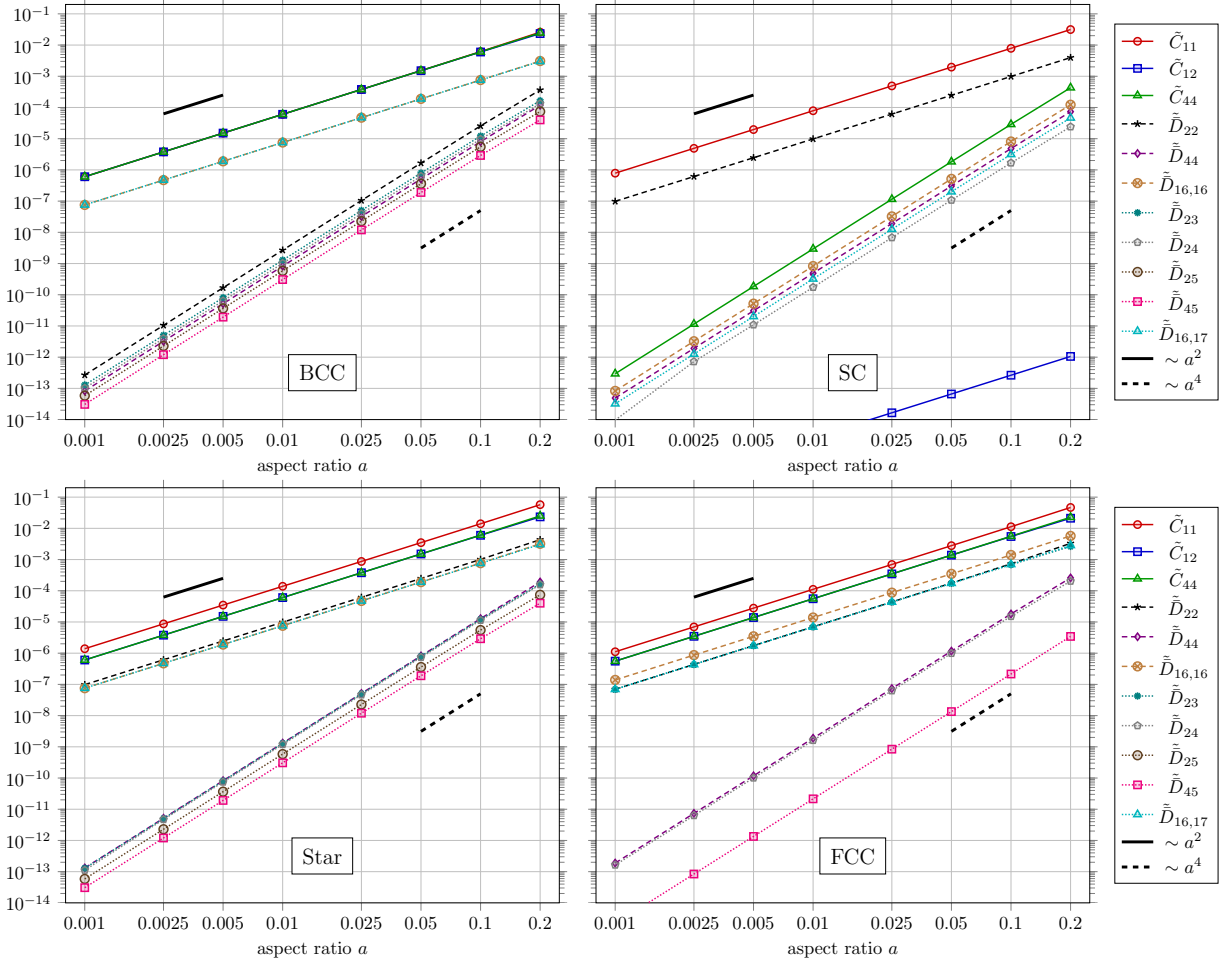


Figure 6: Homogenized effective coefficients of \mathbb{C} and $\bar{\mathbb{D}}$ for BCC, SC, Star & FCC lattice types

second moment of area and bending stiffness scales as $E_b I_b \sim d^4$, see (15). Here, we expect to observe similar scaling behaviors not only for the tensor \mathbb{C} and the effective moduli, but also for the normalized effective second-order constitutive tensor $\bar{\mathbb{D}}$.

To investigate the scaling behavior of the effective constitutive tensors of all 8 microstructures with respect to a , in the following the aspect ratio of the lattice structures is varied as $a = 0.001, \dots, 0.2$, i.e., the beam radii are varied as $r = 0.005, \dots, 1.0$. For the analysis, the cell size $L = 10$ is used, but the cell size is actually not relevant since we always compute the normalized tensor $\bar{\mathbb{D}}$, see (39).

Presentation of results. Now, we proceed with the homogenization of the first- and second-order elastic coefficients of the 8 presented microstructures. The results are summarized in Fig. 6–9, where the coefficients are plotted over the aspect ratio a on log-log-scales. Due to the cubic symmetry of the linear elastic constitutive tensor \mathbb{C} , only the 3 unique components $\tilde{C}_{11}, \tilde{C}_{12}, \tilde{C}_{44}$ are shown, see Fig. 1a. For the normalized second-order constitutive tensor $\bar{\mathbb{D}}^*$, only the 8 non-zero, normalized components $\bar{D}_{212212} = \bar{D}_{22}, \bar{D}_{122122} = \bar{D}_{44}, \bar{D}_{123123} = \bar{D}_{16,16}, \bar{D}_{212313} = \bar{D}_{23}, \bar{D}_{212122} = \bar{D}_{24}, \bar{D}_{212133} = \bar{D}_{25}, \bar{D}_{122133} = \bar{D}_{45}, \bar{D}_{123231} = \bar{D}_{16,17}$ are shown, see Fig. 1b. In Figure 6 and 7 the coefficients are grouped by unit cell type in each plot, in Fig. 8 and 9, they are grouped by the type of coefficient, including the effective Young's modulus E , Poisson ratio ν and shear modulus G , which can all be calculated from \mathbb{C} , see (35). Furthermore, Fig. 10 shows the relative share of the stretching energy over the total potential energy W_b^s/W_b for the computation of the

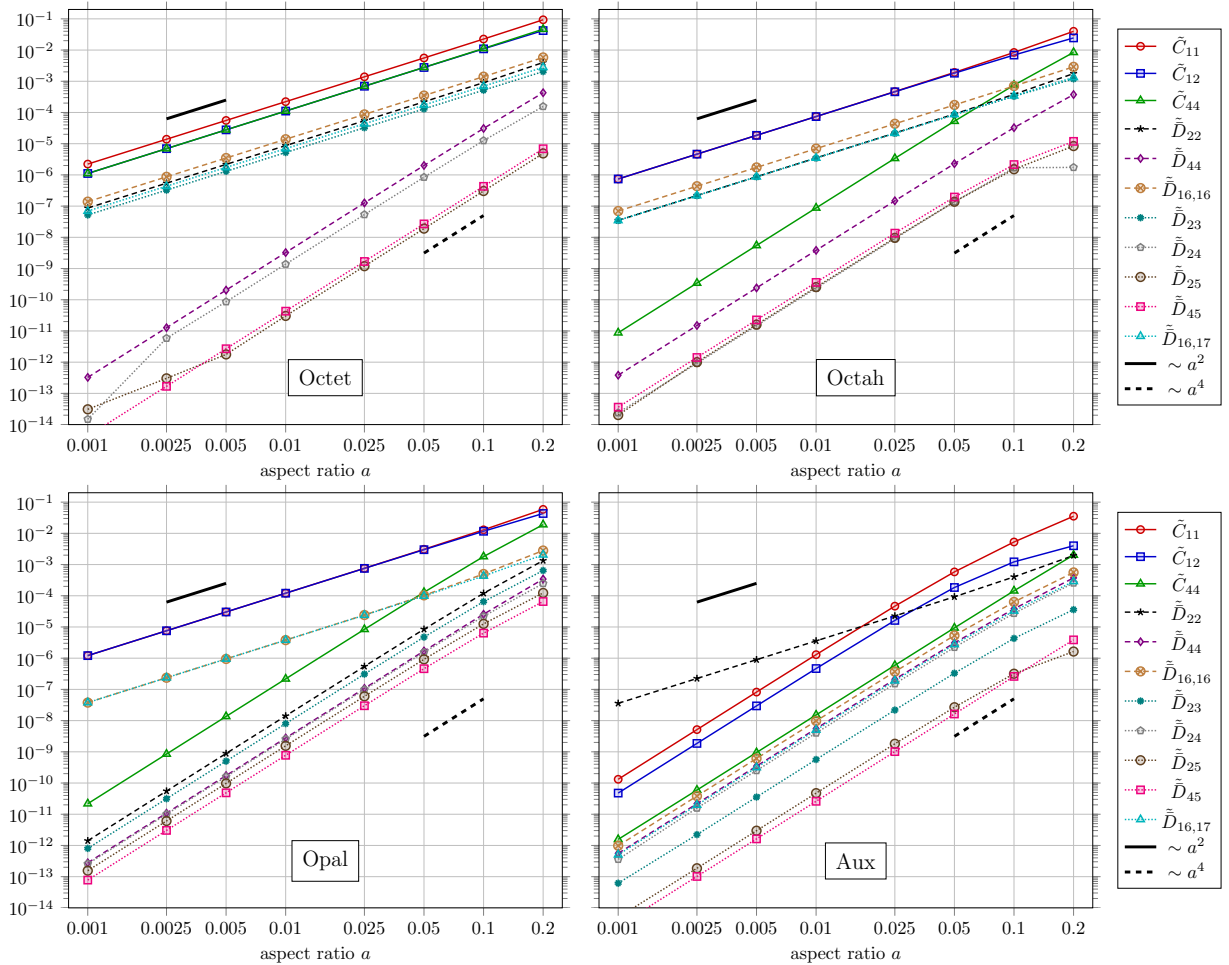


Figure 7: Homogenized effective coefficients of \mathbb{C} and \mathbb{D} for Octet, Octah, Opal & Aux lattice types

diagonal coefficients of \mathbb{C} and \mathbb{D} of all 8 lattice unit cell types, see (22), where values close to 1 indicate stretching-dominated and values close to 0 bending-dominated deformation modes. For the off-diagonal coefficients this ratio is not as straight-forward to compute, since the total energies include contributions from the diagonal coefficients.

Discussion of results for \mathbb{C} . First of all, looking at the coefficients of \mathbb{C} and the moduli in Fig. 8, the typical stretch- or bending-dominated behavior for tensile and shear deformation modes of different microstructures can be observed according to the scaling rates of E and G , which are approximately either of order 2 or 4. For instance, the BCC structure is bending-dominated in tension (E is of order 4), but stretch-dominated in shearing (G is of order 2), while FCC, Star and Octet are always stretch-dominated, and Octahedron, Opal and the auxetic structure always bending-dominated. This classification into stretching- and bending-dominated deformations and microstructures is also validated by the relative share of stretching energy plotted in Fig. 10.

At a first glance, the Poisson's ratios ν remain almost constant over a for all microstructures, except for the auxetic structure, where it increases from $\nu \approx -0.56$ for $a \rightarrow 0$ to $\nu \approx -0.14$ at $a = 0.2$. Since the Poisson's ratio is negative here, it has to be noted that C_{12} is also negative and thus all plots actually show $|C_{12}|$ for Aux (nevertheless, \mathbb{C} is still positive definite). However, when looking at the difference between the Poisson's ratios and their limit values ν_0 for $a \rightarrow 0$, i.e., $|\nu_0 - \nu|$, it can be seen that all differences

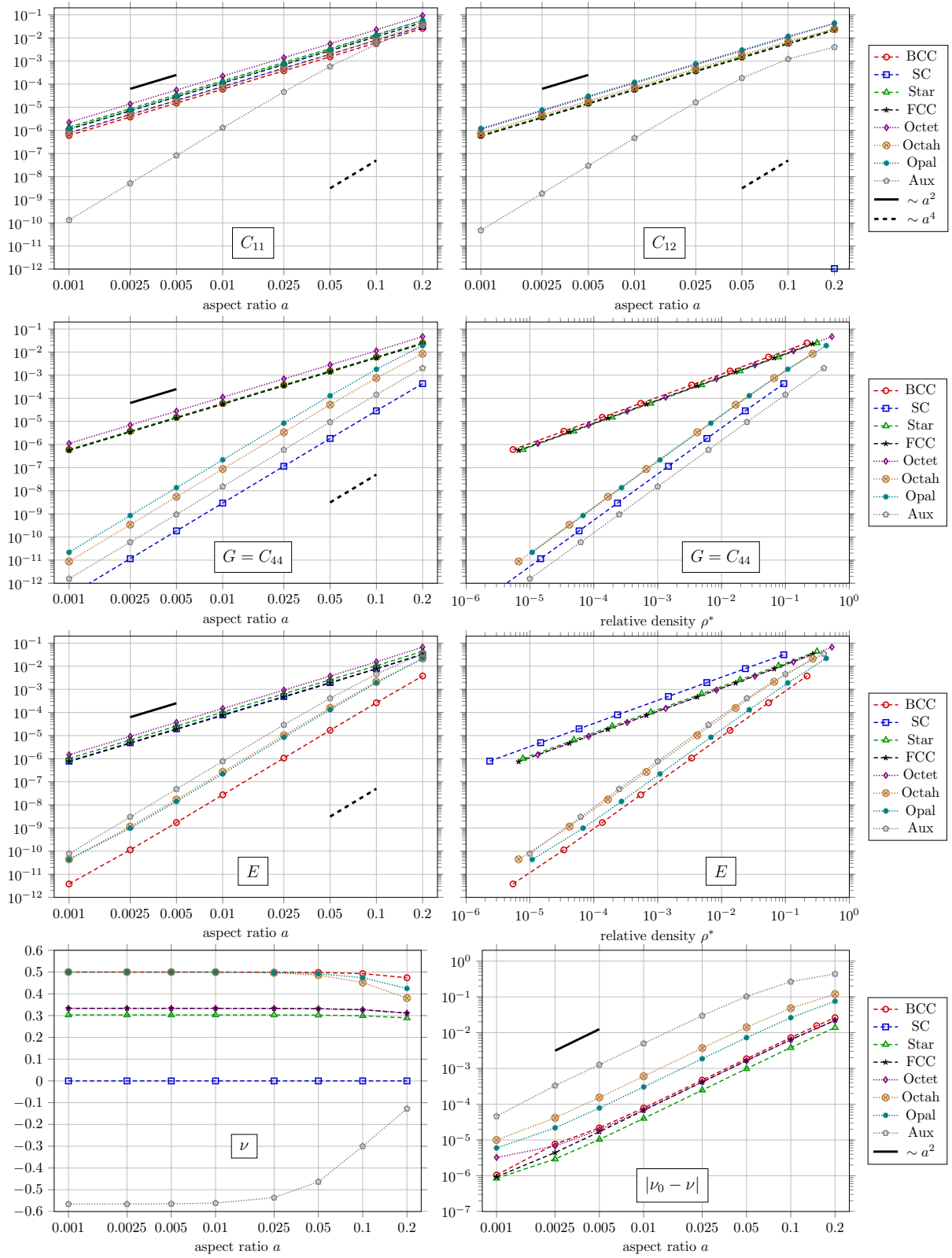


Figure 8: Homogenized effective coefficients of \tilde{C} and moduli for 8 lattice unit cell types, grouped by modulus

Poisson's ratios are of order 2 in a .

As mentioned above, for practical purposes it is often more relevant to relate the effective moduli E and G to the effective density ρ^* , since this allows to compare the mechanical stiffness of different cell types for the same resulting mass of the structure. Thus, those moduli are also plotted over ρ^* in Fig. 8.

Discussion of results for $\bar{\mathbb{D}}$. Now focusing on the normalized second-order coefficients of $\bar{\mathbb{D}}$, we first want to mention again that the coefficient \bar{D}_{11} and all related off-diagonal coefficients \bar{D}_{1i} are zero for all microstructures. Thus, $\bar{\mathbb{D}}$ is only positive semi-definite. Furthermore, it can be noticed that some of the coefficients of the simple cubic (SC) cell, including C_{12} , are many orders of magnitude smaller than the others, see Fig. 6. Though these coefficients scale similarly to the others, it is not clear whether they stem from numerical round-off errors and should be exactly zero, or are just this small. In any case, they can probably be neglected in practical applications.

Looking at the diagonal coefficients in Fig. 9, we observe that \bar{D}_{22} is of second order in a for all cell types except BCC and Opal, \bar{D}_{44} is of fourth order for all cells, and $\bar{D}_{16,16}$ of second order for all cells except SC and Aux. Of the off-diagonal coefficients, \bar{D}_{23} is of second order in a for FCC, Octet and Octah cells (and SC), and of second-order for the other four cells. The coefficients \bar{D}_{24} , \bar{D}_{25} , \bar{D}_{45} are all of fourth order and $\bar{D}_{16,17}$ is generally of second order, except for SC and Aux. It should also be noted that for some cells some of the coefficients can be negative. Thus, all plots show the absolute values of these coefficients, which are \bar{D}_{25} for FCC and Octet, \bar{D}_{45} for Octah, and \bar{D}_{23} and \bar{D}_{25} for Aux. No correlation of the occurrence of negative second-order coefficients with scaling rates or other (first-order) coefficients is apparent.

Overall, the results suggest that the $\tilde{\kappa}_4$ -deformation mode is always related to bending behavior, which also dominates the coupling to other hyperstress components with the off-diagonal coefficients. The $\tilde{\kappa}_2$ and $\tilde{\kappa}_{16}$ modes are mostly related to stretching behavior, except for certain lattice types. However, while $\bar{D}_{16,16}$ and $\bar{D}_{16,17}$ exhibit the same scaling behavior, no correlation between the scaling behavior of \bar{D}_{22} and \bar{D}_{23} can be observed. Again, the general classification into stretching- and bending-dominated behaviors according to the scaling rate in a is confirmed by the relative shares of stretching energy for computing the diagonal coefficients, which are plotted in Fig. 10. However, these behaviors, i.e., whether the cell is stretching- or bending-dominated for a certain type of second-gradient deformation, seem to be uncorrelated with the first-order, linear elastic constitutive coefficients and moduli. This shows that the second gradient theory can cover additional deformation behaviors that are not included in the first-order theory.

Another observation is that the normalized second-order coefficients of $\bar{\mathbb{D}}$ are generally smaller than the first-order coefficients of \mathbb{C} (at least when scaling the same way). However, the actual coefficients of $\bar{\mathbb{D}}$ depend on L^2 , i.e., the larger the cells the larger the second-order coefficients and the more important the second gradient effects. Furthermore, the magnitudes of the coefficients that are of fourth-order in a are generally smaller than the ones of the second-order coefficients. Thus, their contributions to hyperstress and the potential energy are overall smaller and might be less important in a multiscale simulation.

Parameterization of coefficients. Since the homogenized constitutive coefficients of $\tilde{\mathbb{C}}$ and $\tilde{\mathbb{D}}$ depend on the aspect ratio a , see (40), they can be parameterized in terms of a as:

$$\tilde{C}(a) = c_2 a^2 + c_4 a^4, \quad (42)$$

where \tilde{C} here stands for any of the coefficients or moduli obtained. The necessary coefficients c_2, c_4 for these parameterizations are obtained by standard relative least-squares fitting of the data presented above in the interval $a \in [0.005, 0.05]$ and tabulated in Tab. 2. Typically, the relative fitting errors using (42) within this range are smaller than a few percent. Only for the Aux cell, which behaves much less uniformly than the others, compare Fig. 7, errors could be higher for some of the coefficients. Using these coefficients, the actual constitutive tensors for any unit cell type can be computed for given aspect ratio a and cell size L , and then be applied in multiscale simulations with the linear elastic second gradient theory.

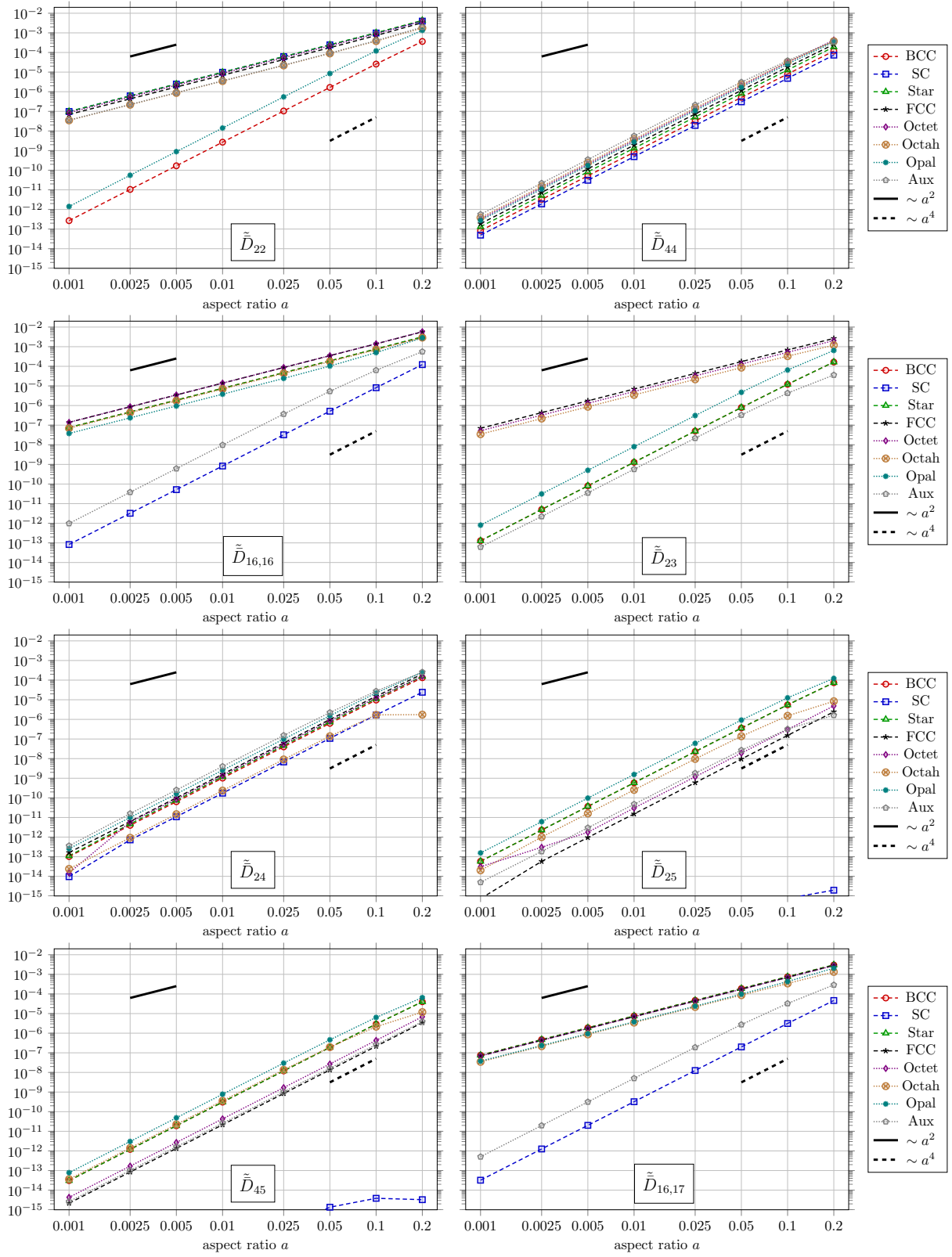


Figure 9: Homogenized effective, normalized coefficients of $\tilde{\mathbb{D}}$ for 8 lattice unit cell types, grouped by modulus

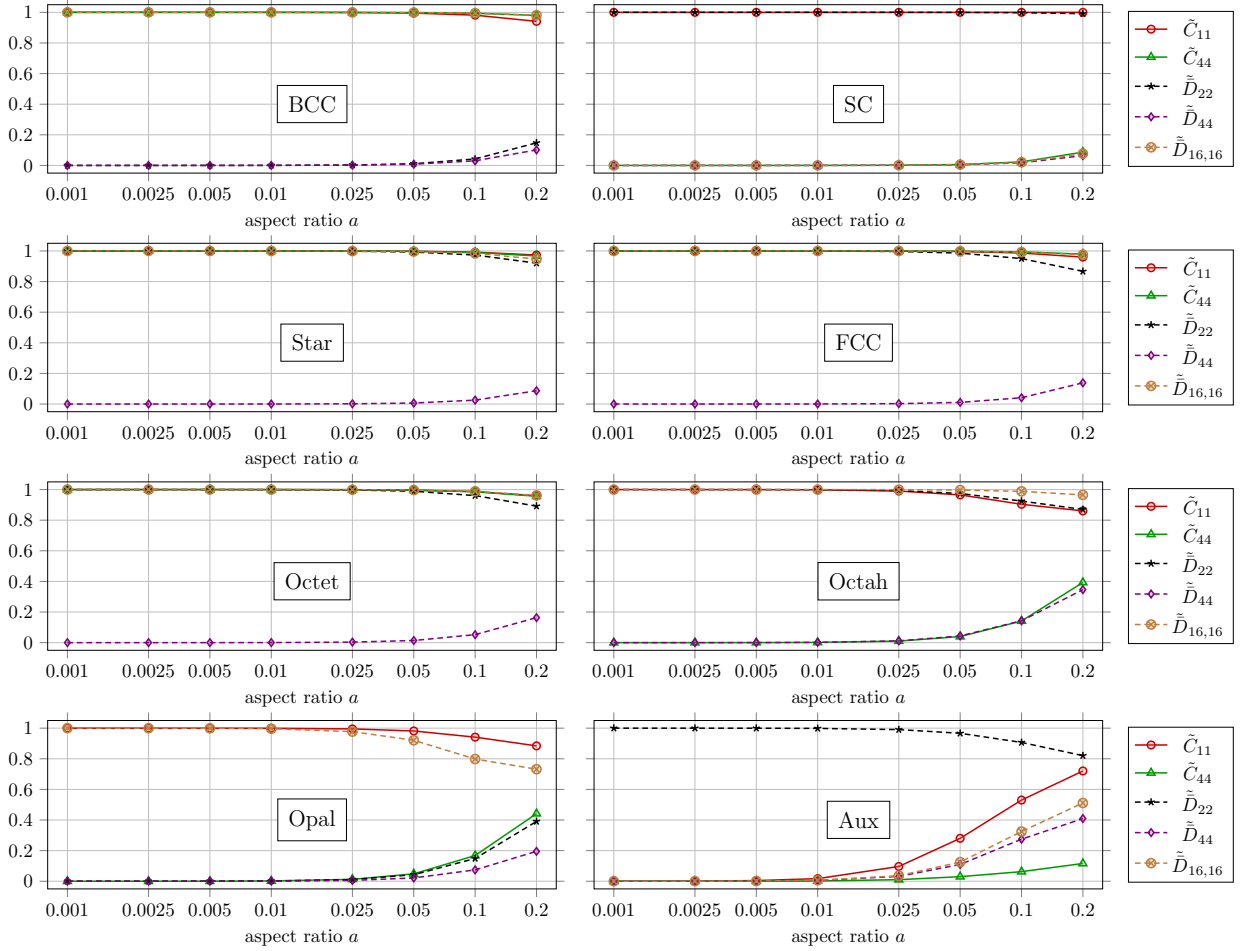


Figure 10: Relative share of stretching energy over total potential energy W_b^s/W_b^b for diagonal coefficients of $\tilde{\mathbb{C}}$ and $\tilde{\mathbb{D}}$ for all 8 unit cells

6. Summary and future work

We have presented a numerical homogenization method for obtaining the effective constitutive parameters of linear elastic second gradient models for cubic beam-lattice metamaterials. The method is based on the microscopic modeling of lattice unit cells as shear-deformable 3D beam structures and homogenization of stresses, hyperstresses and potential energies using periodic boundary conditions with prescribed effective deformations and rotations, which are associated with the rotation part of the polar decomposition of the effective deformation resulting from the second gradient.

This homogenization method was first verified by comparison with full-scale simulations of a sufficiently large, “infinite” lattices with prescribed deformations and then applied to various types of unit cells. It could be shown that the effective second-order constitutive coefficients, which depend on the unit cell size as $\mathbb{D} \sim L^2$ and thus include size effects, also scale with the aspect ratio of the lattice a either as second- or fourth-order polynomials. For this polynomial approximation of the effective constitutive coefficients, the necessary coefficients were also computed and can be used for multiscale simulations by other researchers.

As is well known, the scaling behavior of the effective constitutive coefficients and moduli of lattices can be identified with either stretch- or bending-dominated behaviors in the respective deformations. However, no clear correlation between the scaling behaviors of first-order (linear elastic) and second-order (second gradient) effective constitutive coefficients could be found here. Since scaling behaviors of different coefficients of the same unit cell can be of different order, and first-order coefficients are typically larger in magnitude

	BCC		SC		Star		FCC	
	c_2	c_4	c_2	c_4	c_2	c_4	c_2	c_4
\tilde{C}_{11}	0.6046	0	0.7854	0	1.3900	0	1.1108	0
\tilde{C}_{12}	0.6030	0	0	0	0.6030	0	0.5532	0
\tilde{C}_{44}	0.6046	0	0	0.2918	0.6046	0	0.5554	0
E	0	2.6818	0.7854	0	1.0235	0	0.7406	0
G	0.6046	0	0	0.2918	0.6046	0	0.5554	0
\tilde{D}_{22}	0	0.2635	0.0982	0	0.0982	0	0.0694	0
\tilde{D}_{44}	0	0.0817	0	0.0487	0	0.1304	0	0.1856
$\tilde{D}_{16,16}$	0.0756	0	0	0.0822	0.0756	0	0.1388	0
\tilde{D}_{23}	0	0.1257	0	0	0	0.1257	0.0692	0
\tilde{D}_{24}	0	0.0997	0	0.0171	0	0.1168	0	0.1570
\tilde{D}_{25}	0	0.0570	0	0	0	0.0570	0	-0.0015
\tilde{D}_{45}	0	0.0300	0	0	0	0.0300	0	0.0022
$\tilde{D}_{16,17}$	0.0755	0	0	0.0319	0.0756	0	0.0694	0

	Octet		Octah		Opal		Aux	
	c_2	c_4	c_2	c_4	c_2	c_4	c_2	c_4
\tilde{C}_{11}	2.2216	0	0.7416	0	1.2098	0	0	72.349
\tilde{C}_{12}	1.1064	0	0.7260	0	1.1971	0	0	-17.105
\tilde{C}_{44}	1.1108	0	0	8.2032	0	20.032	0	1.4870
E	1.4812	0	0	24.088	0	20.524	0	58.068
G	1.1108	0	0	8.2032	0	20.032	0	1.4870
\tilde{D}_{22}	0.0868	0	0.0347	0	0	1.3186	0.0358	0
\tilde{D}_{44}	0	0.3184	0	0.3569	0	0.2688	0	0.4600
$\tilde{D}_{16,16}$	0.1388	0	0.0694	0	0.0379	0	0	0.7799
\tilde{D}_{23}	0.0520	0	0.0342	0	0	0.7294	0	-0.0500
\tilde{D}_{24}	0	0.1329	0	0.0203	0	0.2396	0	0.3307
\tilde{D}_{25}	0	-0.0030	0	0.0193	0	0.1415	0	-0.0039
\tilde{D}_{45}	0	0.0043	0	-0.0274	0	0.0711	0	0.0026
$\tilde{D}_{16,17}$	0.0694	0	0.0346	0	0.0378	0	0	0.4028

Table 2: Coefficients for the parameterization of the homogenized constitutive coefficients and moduli of \tilde{C} and \tilde{D} in terms of the aspect ratio a as $\tilde{C}(a) = c_2 a^2 + c_4 a^4$

than the normalized second-order coefficients and often of second-order, it can be expected that the effects of the second gradient models diminish in multiscale simulations with small aspect ratios and small cell size.

To investigate the effects and potential benefits of second gradient elasticity for the multiscale modeling of lattice structures, we are currently extending this work by applying the coefficients obtained here within macroscopic second gradient simulations. However, this not only requires computational methods for the discretization of second gradient elasticity, but also the consideration of the near incompressibility of many of the unit cells, as Poisson's ratios are often very close to 0.5. Furthermore, a validation of the proposed approaches by physical experiments with lattice structures would be desirable and a comparison with other generalized continuum mechanical theories such as micropolar elasticity, too.

Acknowledgments

The author would like to thank Dominik Klein from TU Darmstadt for helping with data and figure preparations.

Declaration of interest

The authors declare that they have no known competing financial interests or personal relationships that could have appeared to influence the work reported in this paper.

Data availability

The data required to reproduce these findings are openly available for download from GitHub repository <https://github.com/CPSHub/sim-data>.

References

- [1] I. Gibson, D. Rosen, and B. Stucker. *Additive Manufacturing Technologies: 3D Printing, Rapid Prototyping, and Direct Digital Manufacturing*. Springer New York, second edition, 2015.
- [2] Jae-Hwang Lee, Jonathan P. Singer, and Edwin L. Thomas. Micro-/Nanostructured Mechanical Metamaterials. *Advanced Materials*, 24(36):4782–4810, 2012.
- [3] J. Plocher and A. Panesar. Review on design and structural optimisation in additive manufacturing: Towards next-generation lightweight structures. *Materials & Design*, 183:108164, December 2019.
- [4] Alexander Großmann, Julian Gosmann, and Christian Mittelstedt. Lightweight lattice structures in selective laser melting: Design, fabrication and mechanical properties. *Materials Science and Engineering: A*, 766:138356, October 2019.
- [5] Xiao Kuang, Jiangtao Wu, Kaijuan Chen, Zeang Zhao, Zhen Ding, Fengjingyang Hu, Daining Fang, and H. Jerry Qi. Grayscale digital light processing 3D printing for highly functionally graded materials. *Science Advances*, 5(5):eaav5790, May 2019.
- [6] S. Babae, J. Shim, J. C. Weaver, E. R. Chen, N. Patel, and K. Bertoldi. 3D Soft Metamaterials with Negative Poisson’s Ratio. *Adv. Mater.*, 25(36):5044–5049, 2013.
- [7] O. Weeger, N. Boddeti, S.-K. Yeung, S. Kaijima, and M.L. Dunn. Digital Design and Nonlinear Simulation for Additive Manufacturing of Soft Lattice Structures. *Additive Manufacturing*, 25:39–49, 2019.
- [8] Julie A. Jackson, Mark C. Messner, Nikola A. Dudukovic, William L. Smith, Logan Bekker, Bryan Moran, Alexandra M. Golobic, Andrew J. Pascall, Eric B. Duoss, Kenneth J. Loh, and Christopher M. Spadaccini. Field responsive mechanical metamaterials. *Science Advances*, 4(12):eaau6419, December 2018.
- [9] Xiaoyu Zheng, William Smith, Julie Jackson, Bryan Moran, Huachen Cui, Da Chen, Jianchao Ye, Nicholas Fang, Nicholas Rodriguez, Todd Weisgraber, and Christopher M. Spadaccini. Multiscale metallic metamaterials. *Nature Materials*, 15(10):1100–1106, October 2016.
- [10] Lorna J. Gibson and Michael F. Ashby. *Cellular Solids: Structure and Properties*. Cambridge Solid State Science Series. Cambridge University Press, May 1997.
- [11] M.F Ashby. The properties of foams and lattices. *Philosophical Transactions of the Royal Society A: Mathematical, Physical and Engineering Sciences*, 364(1838):15–30, January 2006.
- [12] Alain Bensoussan, Jacques-Louis Lions, and George Papanicolaou. *Asymptotic Analysis for Periodic Structures*. American Mathematical Soc., October 2011.
- [13] Tarek I. Zohdi and Peter Wriggers. *An Introduction to Computational Micromechanics*. Lecture Notes in Applied and Computational Mechanics. Springer-Verlag, Berlin Heidelberg, 2005.
- [14] Andrea Vigliotti and Damiano Pasini. Linear multiscale analysis and finite element validation of stretching and bending dominated lattice materials. *Mechanics of Materials*, 46:57–68, March 2012.
- [15] Andrea Vigliotti and Damiano Pasini. Stiffness and strength of tridimensional periodic lattices. *Computer Methods in Applied Mechanics and Engineering*, 229-232:27–43, July 2012.
- [16] Norbert Huber. Connections Between Topology and Macroscopic Mechanical Properties of Three-Dimensional Open-Pore Materials. *Frontiers in Materials*, 5:69, November 2018.
- [17] Ryan M. Latture, Matthew R. Begley, and Frank W. Zok. Design and mechanical properties of elastically isotropic trusses. *Journal of Materials Research*, 33(03):249–263, February 2018.
- [18] José Souza, Alexander Großmann, and Christian Mittelstedt. Micromechanical analysis of the effective properties of lattice structures in additive manufacturing. *Additive Manufacturing*, 23:53–69, October 2018.
- [19] S. Janbaz, F. S. L. Bobbert, M. J. Mirzaali, and A. A. Zadpoor. Ultra-programmable buckling-driven soft cellular mechanisms. *Materials Horizons*, 6:1138, 2019.
- [20] D. W. Rosen. Computer-Aided Design for Additive Manufacturing of Cellular Structures. *Comput. Aided Des. Appl.*, 4(5):585–594, 2007.

- [21] Sang-In Park, David W. Rosen, Seung-Kyum Choi, and Chad E. Duty. Effective Mechanical Properties of Lattice Material Fabricated by Material Extrusion Additive Manufacturing. *Addit. Manuf.*, 1-4:12–23, 2014.
- [22] Sang-In Park and David Rosen. Homogenization of Mechanical Properties for Additively Manufactured Periodic Lattice Structures Considering Joint Stiffening Effects. In *Proceedings of the ASME 2016 IDETC/CIE.*, volume 1A, page V01AT02A036, Charlotte, NC, USA, 2016.
- [23] Carlos M. Portela, Julia R. Greer, and Dennis M. Kochmann. Impact of node geometry on the effective stiffness of non-slender three-dimensional truss lattice architectures. *Extreme Mechanics Letters*, 22:138–148, July 2018.
- [24] Andrew Gross, Panos Pantidis, Katia Bertoldi, and Simos Gerasimidis. Correlation between topology and elastic properties of imperfect truss-lattice materials. *Journal of the Mechanics and Physics of Solids*, 124:577–598, March 2019.
- [25] Bernd Bickel, Moritz Bächer, Miguel A. Otaduy, Hyunho Richard Lee, Hanspeter Pfister, Markus Gross, and Wojciech Matusik. Design and fabrication of materials with desired deformation behavior. In *ACM Transactions on Graphics (TOG)*, volume 29, page 63. ACM, 2010.
- [26] C. Schumacher, B. Bickel, J. Rys, S. Marschner, C. Daraio, and M. Gross. Microstructures to control elasticity in 3D printing. *ACM Transactions on Graphics (TOG)*, 34(4):136, 2015.
- [27] Yingjun Wang, Hang Xu, and Damiano Pasini. Multiscale isogeometric topology optimization for lattice materials. *Computer Methods in Applied Mechanics and Engineering*, 316:568–585, April 2017.
- [28] Yunlong Tang and Yaoyao Fiona Zhao. Multifunctional design of heterogeneous cellular structures. *Structural and Multidisciplinary Optimization*, 58(3):1121–1138, September 2018.
- [29] Yiqiang Wang, Lei Zhang, Stephen Daynes, Hongying Zhang, Stefanie Feih, and Michael Yu Wang. Design of graded lattice structure with optimized mesostructures for additive manufacturing. *Materials & Design*, 142:114–123, March 2018.
- [30] V. Kouznetsova, M. G. D. Geers, and W. a. M. Brekelmans. Multi-scale constitutive modelling of heterogeneous materials with a gradient-enhanced computational homogenization scheme. *International Journal for Numerical Methods in Engineering*, 54(8):1235–1260, July 2002.
- [31] Emilio Barchiesi, Mario Spagnuolo, and Luca Placidi. Mechanical metamaterials: A state of the art. *Mathematics and Mechanics of Solids*, 24(1):212–234, January 2019.
- [32] Holm Altenbach, Wolfgang H. Müller, and Bilal Emek Abali, editors. *Higher Gradient Materials and Related Generalized Continua*, volume 120 of *Advanced Structured Materials*. Springer International Publishing, Cham, 2019.
- [33] Gérard A. Maugin. What Is Generalized Continuum Mechanics (GCM)? In Gérard A. Maugin, editor, *Non-Classical Continuum Mechanics: A Dictionary*, Advanced Structured Materials, pages 15–23. Springer Singapore, Singapore, 2017.
- [34] Francesco dell’Isola and Victor A. Eremeyev. Some Introductory and Historical Remarks on Mechanics of Microstructured Materials. In Francesco dell’Isola, Victor A. Eremeyev, and Alexey Porubov, editors, *Advances in Mechanics of Microstructured Media and Structures*, volume 87, pages 1–20. Springer International Publishing, Cham, 2018.
- [35] D. C. C. Lam, F. Yang, A. C. M. Chong, J. Wang, and P. Tong. Experiments and theory in strain gradient elasticity. *Journal of the Mechanics and Physics of Solids*, 51(8):1477–1508, August 2003.
- [36] J. Y. Chen, Y. Huang, and M. Ortiz. Fracture analysis of cellular materials: A strain gradient model. *Journal of the Mechanics and Physics of Solids*, 46(5):789–828, May 1998.
- [37] H. Gao, Y. Huang, W. D. Nix, and J. W. Hutchinson. Mechanism-based strain gradient plasticity—I. Theory. *Journal of the Mechanics and Physics of Solids*, 47(6):1239–1263, April 1999.
- [38] C. Pideri and P. Seppecher. A second gradient material resulting from the homogenization of an heterogeneous linear elastic medium. *Continuum Mechanics and Thermodynamics*, 9(5):241–257, October 1997.
- [39] Ragnar Larsson and Stefan Diebels. A second-order homogenization procedure for multi-scale analysis based on micropolar kinematics. *International Journal for Numerical Methods in Engineering*, 69(12):2485–2512, March 2007.
- [40] N. Auffray, R. Bouchet, and Y. Bréchet. Strain gradient elastic homogenization of bidimensional cellular media. *International Journal of Solids and Structures*, 47(13):1698–1710, June 2010.
- [41] Ibrahim Goda and Jean-François Ganghoffer. Construction of first and second order grade anisotropic continuum media for 3D porous and textile composite structures. *Composite Structures*, 141:292–327, May 2016.
- [42] K. Berkache, S. Deogekar, I. Goda, R. C. Picu, and J. F. Ganghoffer. Construction of second gradient continuum models for random fibrous networks and analysis of size effects. *Composite Structures*, 181:347–357, December 2017.
- [43] H. Yang, B. E. Abali, W. H. Müller, and D. Timofeev. Determination of Metamaterial Parameters by Means of a Homogenization Approach Based on Asymptotic Analysis. *Continuum Mechanics and Thermodynamics*, October 2019.
- [44] Zineeddine Louna, Ibrahim Goda, and Jean-François Ganghoffer. Homogenized strain gradient remodeling model for trabecular bone microstructures. *Continuum Mechanics and Thermodynamics*, 31(5):1339–1367, September 2019.
- [45] Łukasz Kaczmarczyk, Chris J. Pearce, and Nenad Bićanić. Scale transition and enforcement of RVE boundary conditions in second-order computational homogenization. *International Journal for Numerical Methods in Engineering*, 74(3):506–522, 2008.
- [46] S. Forest and D. K. Trinh. Generalized continua and non-homogeneous boundary conditions in homogenisation methods. *ZAMM - Journal of Applied Mathematics and Mechanics / Zeitschrift für Angewandte Mathematik und Mechanik*, 91(2):90–109, 2011.
- [47] Céline Florence and Karam Sab. Overall ultimate yield surface of periodic tetrakaidecahedral lattice with non-symmetric material distribution. *Journal of Materials Science*, 40(22):5883–5892, November 2005.
- [48] Céline Florence and Karam Sab. A rigorous homogenization method for the determination of the overall ultimate strength of periodic discrete media and an application to general hexagonal lattices of beams. *European Journal of Mechanics - A/Solids*, 25(1):72–97, January 2006.
- [49] F. Dos Reis and J. F. Ganghoffer. Construction of micropolar continua from the asymptotic homogenization of beam

- lattices. *Computers & Structures*, 112-113:354–363, December 2012.
- [50] Marcus Yoder, Lonny Thompson, and Joshua Summers. Size effects in lattice structures and a comparison to micropolar elasticity. *International Journal of Solids and Structures*, 143:245–261, June 2018.
- [51] Y. Rahali, I. Giorgio, J.-F. Ganghoffer, and F dell’Isola. Homogenization à la Piola produces second gradient continuum models for linear pantographic lattices. *International Journal of Engineering Science*, 97:148–172, December 2015.
- [52] Sergei Khakalo, Viacheslav Balabanov, and Jarkko Niiranen. Modelling size-dependent bending, buckling and vibrations of 2D triangular lattices by strain gradient elasticity models: Applications to sandwich beams and auxetics. *International Journal of Engineering Science*, 127:33–52, June 2018.
- [53] Sergei Khakalo and Jarkko Niiranen. Anisotropic strain gradient thermoelasticity for cellular structures: Plate models, homogenization and isogeometric analysis. *Journal of the Mechanics and Physics of Solids*, page 103728, September 2019.
- [54] Raphaël N. Glaesener, Claire Lestringant, Bastian Telgen, and Dennis M. Kochmann. Continuum models for stretching- and bending-dominated periodic trusses undergoing finite deformations. *Int. J. Solids Struct.*, 2019.
- [55] A. Sridhar, V. G. Kouznetsova, and M. G. D. Geers. A general multiscale framework for the emergent effective elastodynamics of metamaterials. *Journal of the Mechanics and Physics of Solids*, 111:414–433, February 2018.
- [56] K. El Nady, F. Dos Reis, and J. F. Ganghoffer. Computation of the homogenized nonlinear elastic response of 2D and 3D auxetic structures based on micropolar continuum models. *Composite Structures*, 170:271–290, June 2017.
- [57] R. D. Mindlin. Micro-structure in linear elasticity. *Archive for Rational Mechanics and Analysis*, 16(1):51–78, January 1964.
- [58] R.D. Mindlin. Second gradient of strain and surface-tension in linear elasticity. *International Journal of Solids and Structures*, 1(4):417–438, November 1965.
- [59] O. Weeger, S.-K. Yeung, and M.L. Dunn. Isogeometric collocation methods for Cosserat rods and rod structures. *Computer Methods in Applied Mechanics and Engineering*, 316:100–122, 2017.
- [60] Paul Fischer, Markus Klassen, Julia Mergheim, Paul Steinmann, and Ralf Müller. Isogeometric analysis of 2D gradient elasticity. *Computational Mechanics*, 47(3):325–334, March 2011.
- [61] Albrecht Bertram. Compendium on Gradient Materials, December 2017.
- [62] E. Reissner. On finite deformations of space-curved beams. *Zeitschrift für angewandte Mathematik und Physik ZAMP*, 32(6):734–744, 1981.
- [63] J. C. Simo. A finite strain beam formulation. The three-dimensional dynamic problem. Part I. *Computer Methods in Applied Mechanics and Engineering*, 49(1):55–70, 1985.
- [64] Xi Yuan, Yoshihiro Tomita, and Tomoaki Andou. A micromechanical approach of nonlocal modeling for media with periodic microstructures. *Mechanics Research Communications*, 35(1):126–133, January 2008.
- [65] Daniela Addessi, Maria Laura De Bellis, and Elio Sacco. A micromechanical approach for the Cosserat modeling of composites. *Meccanica*, 51(3):569–592, March 2016.